Posted on Authorea 7 Jul 2022 — The copyright holder is the author/funder. All rights reserved. No reuse without permission. — https://doi.org/10.22541/au.165720844.43317885/v1 — This a preprint and has not been peer reviewed. Data may be preliminary.

Phase-field modeling of near-neutral pH stress corrosion crack initiation life in underground pipelines

Edel R. Martnez[1] and Solomon Tesfamariam[1]

[1]The University of British Columbia Okanagan

July 7, 2022

Abstract

A unified phase-field theory is introduced to describe crack initiation and early crack growth due to pitting corrosion of pipelines in contact with near-neutral pH groundwater. The model incorporates a formulation that accounts for stochastic corrosion-induced crack nucleation events at pit sites. This approach supplies a modeling framework to handle the combined effects of electrochemical transformation of the original metal, hydrogen diffusion and resulting embrittlement of the original metal, and mechanical stresses. This is a robust computational approach to tracking the evolving metalelectrolyte interface and embrittlement regions. It was confirmed that dissolved hydrogen into the material promotes crack initiation over a wide potential range and that pitting corrosion, as a precursor of stress corrosion cracking, has a recognizable influence on strength over time. It is expected that this work provides the ground for modeling the pit-to-crack transition required to effectively control very slow crack-in-colonies in pipelines.

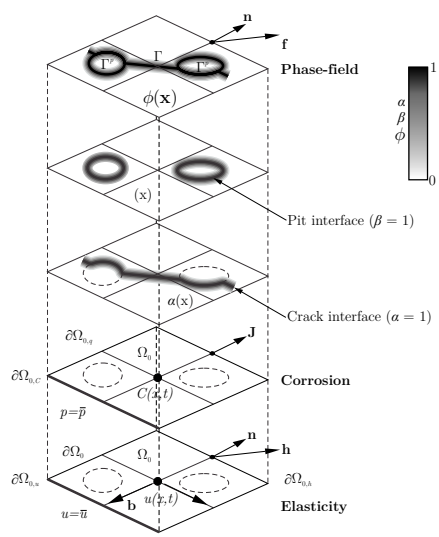

Posted on Authorea 7 Jul 2022 — The copyright holder is the author/funder. All rights reserved. No reuse without permission. — https://doi.org/10.22541/au.165720844.43317885/v1 — This a preprint and has not been peer reviewed. Data may be preliminary.

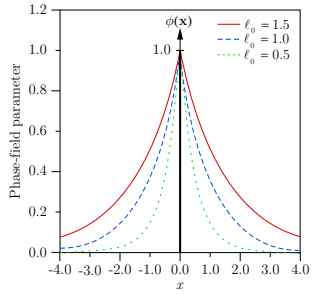

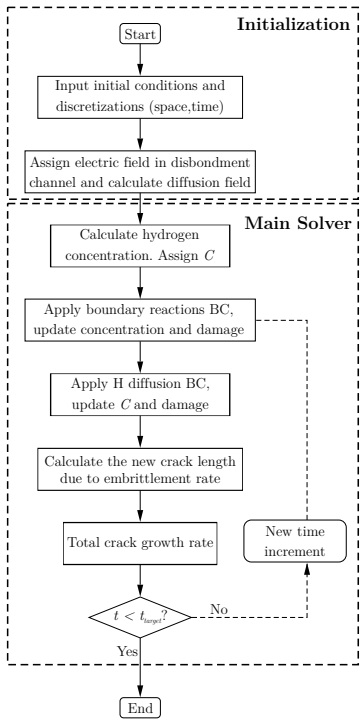

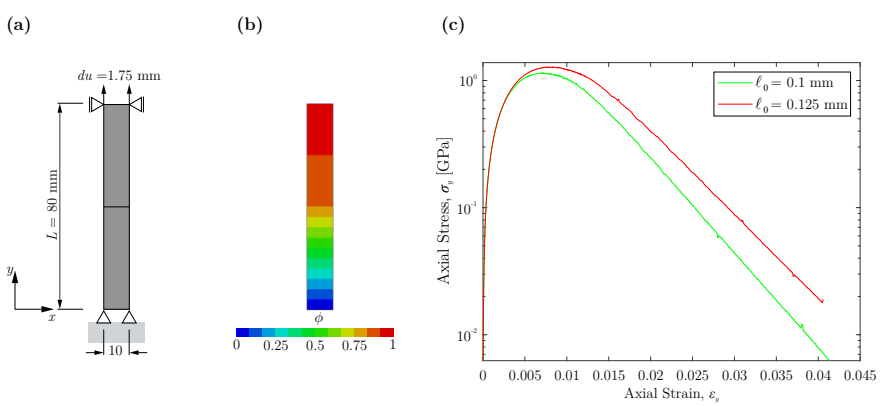

Posted on Authorea 7 Jul 2022 — The copyright holder is the author/funder. All rights reserved. No reuse without permission. — https://doi.org/10.22541/au.165720844.43317885/v1 — This a preprint and has not been peer reviewed. Data may be preliminary.

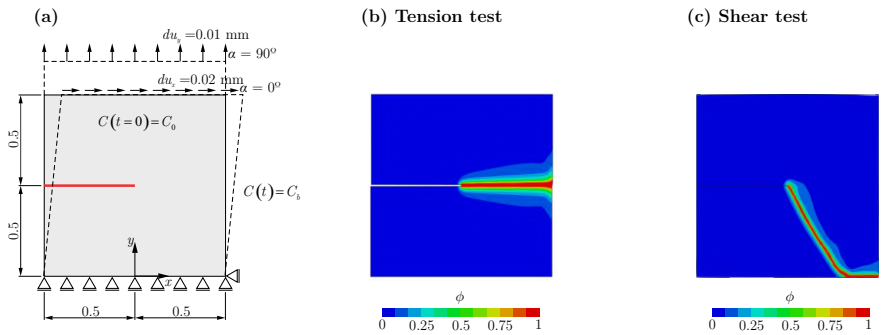

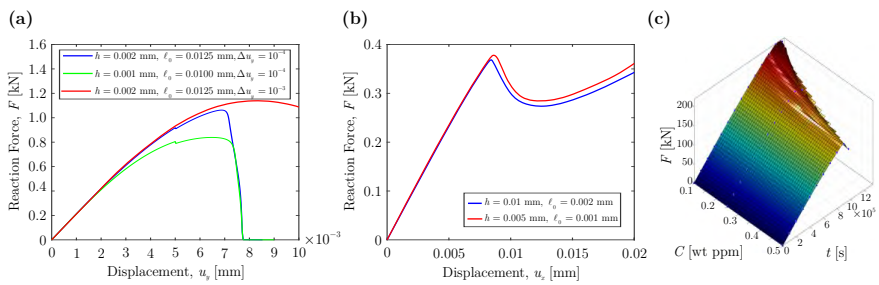

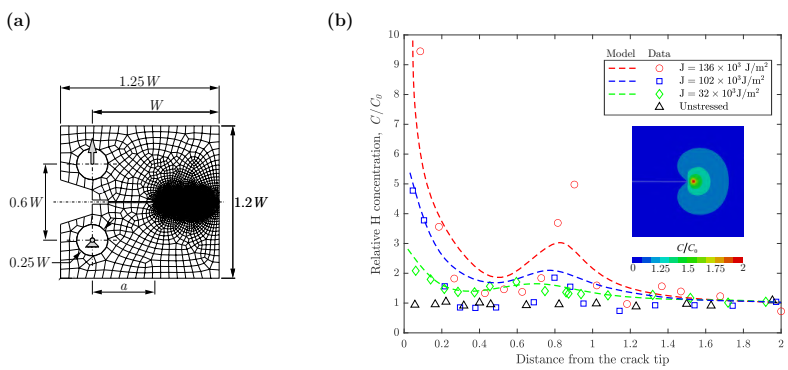

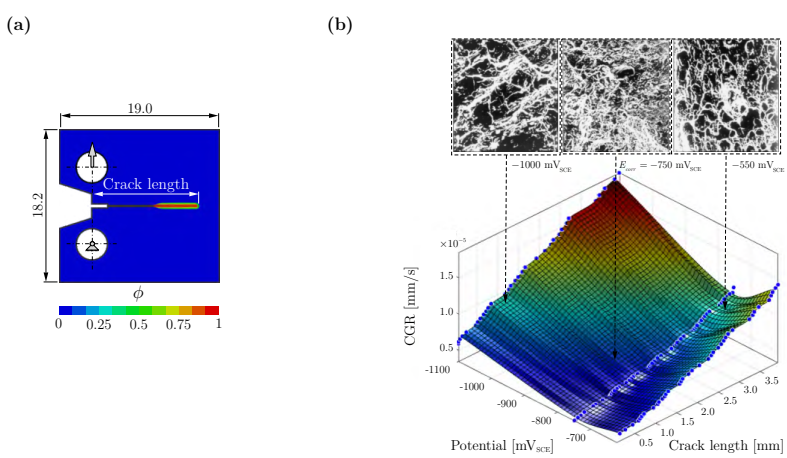

Posted on Authorea 7 Jul 2022 — The copyright holder is the author/funder. All rights reserved. No reuse without permission. — https://doi.org/10.22541/au.165720844.43317885/v1 — This a preprint and has not been peer reviewed. Data may be preliminary.

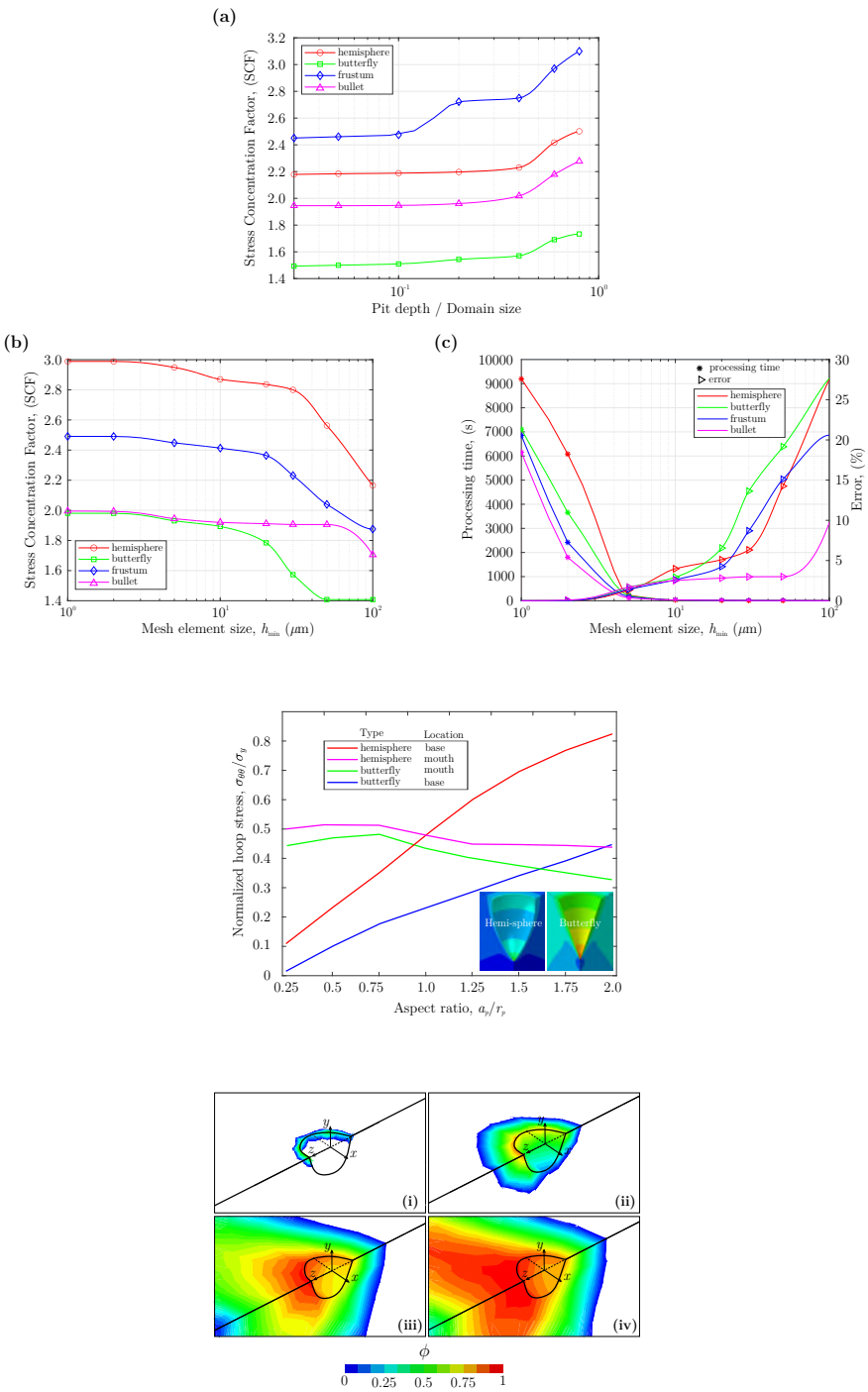

Posted on Authorea 7 Jul 2022 — The copyright holder is the author/funder. All rights reserved. No reuse without permission. — https://doi.org/10.22541/au.165720844.43317885/v1 — This a preprint and has not been peer reviewed. Data may be preliminary.

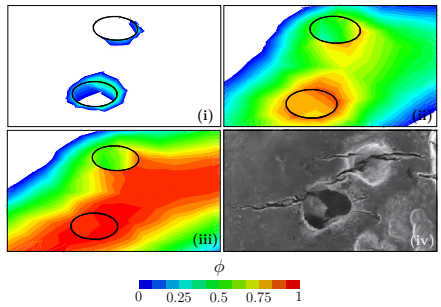

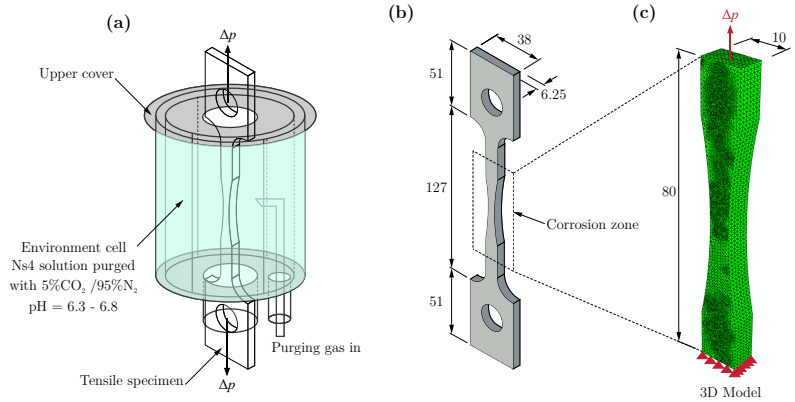

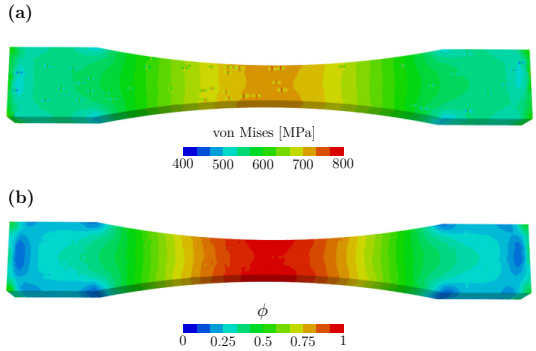

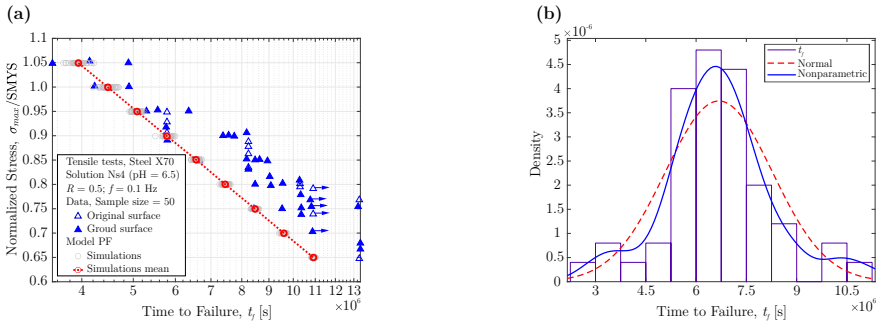

Posted on Authorea 7 Jul 2022 — The copyright holder is the author/funder. All rights reserved. No reuse without permission. — https://doi.org/10.22541/au.165720844.43317885/v1 — This a preprint and has not been peer reviewed. Data may be preliminary.

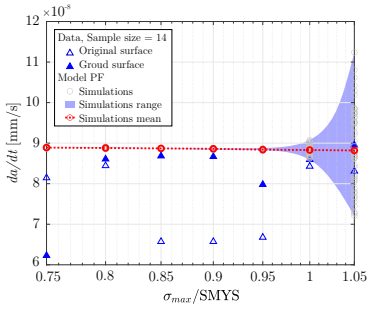

Phase-field modeling of near-neutral pH stress corrosion crack initiation life in underground pipelines

Edel R. Martínez[a], Solomon Tesfamariam[a,1,*]

[a]*School of Engineering, The University of British Columbia, Okanagan campus, Kelowna, BC, Canada*

Abstract

A unified phase-field theory is introduced to describe crack initiation and early crack growth due to pitting corrosion of pipelines in contact with near-neutral pH groundwater. The model incorporates a formulation that accounts for stochastic corrosion-induced crack nucleation events at pit sites. This approach supplies a modeling framework to handle the combined effects of electrochemical transformation of the original metal, hydrogen diffusion and resulting embrittlement of the original metal, and mechanical stresses. This is a robust computational approach to tracking the evolving metal–electrolyte interface and embrittlement regions. It was confirmed that dissolved hydrogen into the material promotes crack initiation over a wide potential range and that pitting corrosion, as a precursor of stress corrosion cracking, has a recognizable influence on strength over time. It is expected that this work provides the ground for modeling the pit-to-crack transition required to effectively control very slow crack-in-colonies in pipelines.

Keywords: phase-field, hydrogen embrittlement, crack-in-colonies, stress corrosion cracking, multiphysics.

1. Introduction

Predicting the evolution and behaviour of colonies of stress corrosion cracking (SCC) can play a critical role to improve SCC resistance of steels, develop prevention techniques, optimization of the performance, reliability, and life cycle costs of oil and gas pipelines [1–5]. Colonies of SCC may contain thousands of closely spaced cracks often aligned with the axial direction of the pipeline [1, 2, 6–8]. Field investigations in transgranular SCC reported that approximately 95% of cracks remained dormant throughout the lifetime of the pipeline [9, 10]. This aspect has been mainly attributed to a reduced rate of dissolution at the crack tip in the depth direction [11, 12]. Although crack dormancy is manifested [1, 12–16], the corrosion process could continue, and if so, it can increase blunting and stagnate the solution inside the crack, thereby affecting the probability of re-activation [15]. Evidence also pointed out the existence of two sequential mechanics for the initiation and early-crack growth of transgranular SCC; first, the anodic dissolution (AD) leading to pitting [17–19] and then the hydrogen embrittlement (HE) by means of acidification within these pits [20, 21]. The underlying material toughness in the vicinity of the corrosion pit can be reduced due to the HE process and corrosion products can lead to a buildup of tensile stresses [21, 22]. The description of the occluded chemistry effect and micro-cracks sites are essential to provide electrochemical formalities of the mechanisms associated with AD and HE [21, 22]. Pending for a suitable integration of the effects produced by the occluded chemistry, cyclic loads, and nucleation of micro-cracks sites the colony evolution remains poorly understood [21–26]. Solving this strongly coupled problem is very challenging because it requires predicting the rate-determining step under multiple physicochemical processes including mass transport of species to and from the crack tip; the oxidation or reduction reactions at the crack tip, and the dynamic strain processes at the crack tip [24, 27].

A plausible solution for estimating the behavior of the colony under these multiple conditions is to blend statistical and phenomenological models [19, 28, 29]. Statistical modeling raised from observation of phenomena that occurs

*Corresponding author

Email address: solomon.tesfamariam@ubc.ca (Solomon Tesfamariam)

[1]Professor

and follows certain statistical models [22, 30–38]. Examples include modeling pit nucleation by nonhomogeneous linear growth Markov process [39, 40], the nucleation of cracks as a Poisson distribution [21, 29], the individual crack length as a Gamma distribution [21, 29], and the initial crack trajectory as a Winner process. Overall, a major drawback of statistical models is that they cannot provide any explanation to the various underlying physics [19, 28, 41]. Phenomenological models, *vis-à-vis* experimental-based statistical modeling, provide the structure to assess the cracking susceptibility for a wide range of key internal and external variables [1, 28, 33, 42, 43]. A variety of computational algorithms have been proposed to individually simulate these stages including non-linear FEM [26], the finite volume method [44], extended FEM [45, 46], cohesive zone model [47, 48], cellular automata [49], peridynamics [50, 51], among others. There are a number of comprehensive reviews on numerical modeling applications for pitting corrosion (e.g., [52]), hydrogen-assisted cracking (e.g., [53]), and corrosion fatigue (e.g., [54]) that the reader could refer to. The quantification of physicochemical processes at the underlying level, and the introduction of various interacting variables and time dependence, pose a significant challenge [55–57], especially for the assessment of crack growth in the short crack domain.

A relatively recent phenomenological model grounded on a diffusive approach, so-called the phase-field model (PFM), appeared to alleviate major issues associated with discrete fracture modeling. In the PFM, the sharp crack topology is geometrically regularized as a damage localization band with an incorporated length scale. Since the material interface is tracked implicitly by solving the dynamic governing equations there is no need to assign boundary conditions along with the moving interface, which enables flexible crack propagation and tracking while avoiding mesh adaption to the crack surfaces. Thus, it offers an excellent balance between physics replicability and computational cost. The benefit of such an approach in multiphysics problems can be far-reaching. It has been used in modeling microstructural features of materials processing such as dendrite growth [58, 59], solidification [60, 61], and phase transformation [62], see for a comprehensive review [63–65]. A number of studies have begun to examine the capability of the PFM to solve the problem of environment-assisted cracking in metals including hydrogen-assisted cracking [66–68] and the AD mechanism as crack driving force [69–75]. Ståhle and Hansen [69] modeled SCC colonies by means of spatiotemporal waves but concerns in the solution arise due to the sensitivity of the solution to the initial conditions. By means of the Kim-Kim-Suzuki (KKS) PFM [76], Mai et al. [70] simulated pitting corrosion and later Mai and Soghrati [71] extended the approach to simulate the initiation of SCC from surface pits. The KKS PFM assumes that every material point in the corroding system is composed of coexisting solid and liquid phases. They recommended that a solution to simulate both activation- and diffusion-controlled mechanisms can be achieved by adjusting the interface kinetics parameter. Nguyen et al. [73] combined phase-field simulation with a full-scale image processing technique in order to capture more realistically the crack onset and damage mechanism associated with SCC in an Inconel 600 alloy sample containing a crack network. Cui et al. [75] modeled both pitting corrosion and SCC using a time dependence behavior of the current density and the interface kinetics parameter. Moreover, they included the effect of mechanical straining on the corrosion rate by considering a mechanochemical term that affects the corrosion current density.

2. Problem statement

Consider a body with domain Ω that has a number of pits nucleated in the exterior surface. Here we are interested in simulating the pit growth kinetics, the transition from pits to cracks, and the growth rate of cracks in the short crack domain using a phase-field paradigm with statistically variable input parameters. For this, the boundary value problem of the interplay among corrosion evolution, mechanical damage, and elastic deformation is presented in Fig. 1. Starting at the bottom in Fig. 1 we have: corrosion dissolution induced mechanical damage near the corrosion front, then HE induced mechanical damage near the fracture process zone.

The bottom of Fig. 1 presents the reference configuration of a cracking solid $\Omega_0 \in \mathbb{R}^D$ ($D = 1, 2, 3$). The external boundary of Ω_0 is denoted by $\partial\Omega_0 \in \mathbb{R}^{D-1}$ of outward unit normal vector $\mathbf{n}$ subjected to the displacement field $\mathbf{u}$ (at $\partial\Omega_{0,u}$) and traction $\mathbf{h}$ (at $\partial\Omega_{0,h}$). Assume that the solid is subjected to a specific body force field per unit volume $\mathbf{b}$. Moreover, as part of initial boundary conditions the hydrogen flux $\mathbf{J}$ (at $\partial\Omega_q$) and concentration $\mathbf{C}$ (at $\partial\Omega_C$) are prescribed. $\partial\Omega_{0,u}$ and $\partial\Omega_{0,q}$ are Dirichlet type boundary conditions. $\partial\Omega_{0,h}$ and $\partial\Omega_{0,C}$ are Neumann-type boundary conditions. The crack domains inside the solid are represented by the discrete internal discontinuity Γ. The internal interfaces of pits are collectively denoted by Γ^p. The two top planes of this figure show the scalar phase-field $\phi(\mathbf{x}, t)$ and the interfaces by a fixed scalar function $\beta(\mathbf{x})$, which are a consequence of the solid deformation. It follows that

Nomenclature

Physics Constants	
C	bulk hydrogen concentration
D	diffusion coefficient
E	Young's modulus
g	degradation function
h	finite element size
k	small parameter
T	temperature
t_f	time to failure
$\bar{V}_{\mathrm{H}}$	partial molar volume
$\mathcal{R}$	universal gas constant
ℓ_0	length scale parameter
G_c	critical energy release
Greek Symbols	
β	pit interfaces scalar function
χ	damage coefficient
Δg_b^0	Gibbs free energy difference
Δu	deformation
Γ	crack domain
ν	Poisson's ratio
Ω	solid domain
ϕ	scalar phase-field
ψ_0	strain energy density
Ψ	total potential energy functional
ψ	bulk energy
ρ	density
θ	hydrogen coverage
γ_l	crack surface density function
Vectors	
$\mathbf{b}$	body force field per unit volume
$\mathbf{C}$	concentration
$\mathbf{h}$	traction field
$\mathbf{J}$	hydrogen flux
$\mathbf{n}$	unit normal vector
$\mathbf{u}$	displacement field

$\phi(x) \in [0, 1]$ can be described as a diffuse interface of Γ. The localization band is not known *a priori* but rather, it is determined and automatically updated. The width of the localization band is described through a length scale parameter ℓ_0.

The mathematical framework of the PFM is developed from the consideration that the free energy of the system is a functional of a set of field variables and their gradients. This free energy is described thermodynamically as a decreasing function depending on the metal embrittlement process. From the minimization of the free energy, the governing equations of the phase-field variables are derived and the problem is implemented using finite elements. The Cahn-Hilliard equations are employed for governing mass transport.

3. A multistage SCC phase-field theory

In this section, we briefly review the unified phase-field theory within the framework of corrosion-fracture couplings. The coupled phase-field includes two important interactions (see Fig. 1): (i) diffusion and phase-field interact to model the diffusivity change due to material property degradation; and (ii) corrosion product in the steel interacts with mechanical straining fracture including the effects of corrosion damage due to dissolved hydrogen.

3.1. Phase-field fracture model

The behavior of all the cracks in the colony are modeled using the phase-field paradigm. The non-conserved phase-field parameter ϕ varies between zero (no damaged/uncracked) and one (fully damaged/cracked). This variable reduces both the real stress and stiffness of the material. If function $\phi(x)$ describes the damage, a sharp crack shown in Fig. 2b is a Dirac delta function. Its value is zero everywhere except $x = 0$, where $\phi(0) = 1$. Variable $\phi(x) \in [0, 1]$ is the crack phase-field function, thus

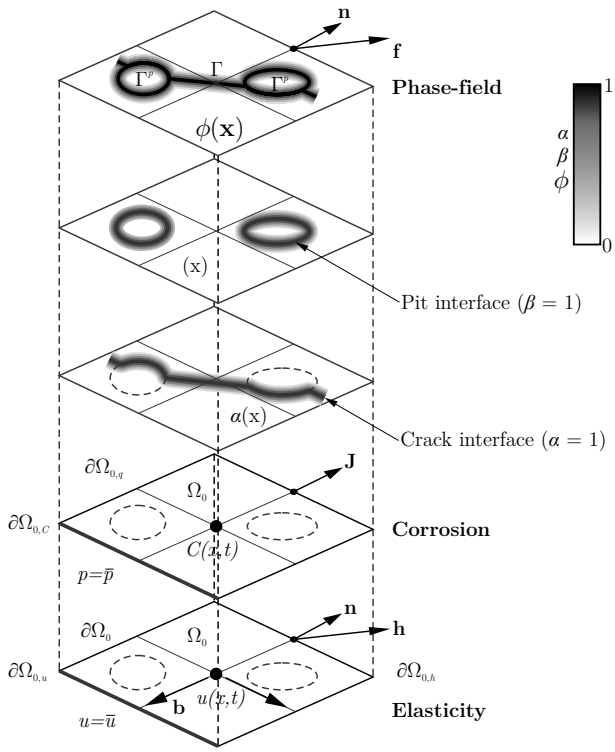

Figure 1: Schematic representation of the coupled phase-field theory with a diffused approximation of cracks and interfaces and the interaction of deformation, phase-field, and mass transport. It is shown an illustration the details of the phase-field variable in pits $\beta(\mathbf{x})$ and cracks $\phi(\mathbf{x})$.

.

$$\phi(x) = \begin{cases} 1 \text{ if } x = 0 \\ 0 \text{ if } x \neq 0 \end{cases} \tag{1}$$

which is referred to as the crack phase-field order parameter, with $\phi = 0$ and $\phi = 1$ respectively denoting the intact and fully broken states of the material. For one-dimensional case, the non-smooth crack phase-field (1) can be approximated by the exponential function,

$$\phi(x) = \exp\left(\frac{-|x|}{\ell_0}\right), \tag{2}$$

where x is the distance, and ℓ_0 is length scale parameter which controls the spread of damage. $\phi(x)$ represents the regularized or diffuse crack topology. By $\ell_0 \to 0$ the sharp case is recovered. Eq. (2) has the property $\phi(0) = 1$ and at the limits $\phi(\pm\infty) = 0$. The interrelationship between the ℓ_0 and $\phi(x)$ in Eq. (2) is schematically shown in Fig. 2 where the crack front is in a direction perpendicular to plane of the figure.

It is the solution for the homogeneous differential equation [77]:

$$\phi(x) - \ell_0^2 \phi''(x) = 0 \quad \text{in} \quad \Omega_0, \tag{3}$$

subject to the Dirichlet-type boundary condition shown above. The variational principle of strong form is written as:

$$\phi = \text{Arg}\left\{\inf_{\phi \in W} I(\phi)\right\}, \tag{4}$$

where

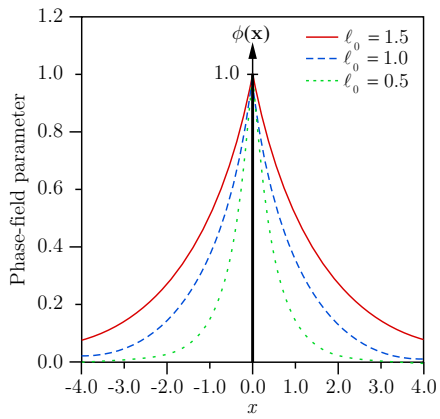

Figure 2: Diffuse crack at $x = 0$ modeled with function (2) and length scale parameter ℓ_0. For reference the sharp crack for $\phi = 1$ is shown.

$$I(\phi) = \frac{1}{2}\int_{\Omega}\left(\phi^2 + \ell_0^2\nabla\phi^2\right)\mathrm{d}V, \tag{5}$$

and $W = \{\phi|\,\phi(0) = 0,\ \phi(\pm\infty) = 0\}$. Now observe that the integration over volume $\mathrm{d}V = \Gamma\mathrm{d}x$ gives $I(\phi = \exp(-|x|/\ell_0)) = \ell_0\Gamma$. Thus, the fracture surface is related to the crack length parameter. As a consequence, we may introduce a fracture surface density with the help of the phase-field function by:

$$\Gamma(\phi) = \frac{1}{\ell_0}I(\phi) = \int_{\Omega}\left(\frac{1}{2\ell_0}\phi^2 + \frac{\ell_0}{2}|\nabla\phi|^2\right)\mathrm{d}V = \int_{\Omega}\gamma_l(\phi,\nabla\phi)\,\mathrm{d}V \tag{6}$$

where $\gamma_l(\phi,\nabla\phi)\,\mathrm{d}V$ is the crack surface density function in 1D. Similarly, in multiple dimensions it can be expressed as:

$$\gamma_l(\phi,\nabla\phi) = \frac{1}{2\ell_0}\phi^2 + \frac{\ell_0}{2}|\nabla\phi|^2, \tag{7}$$

The fracture energy due to the formation of a crack is then approximated as,

$$\int_{\Gamma} G_c(\theta)\mathrm{d}S \approx \int_{\Omega} G_c(\theta)\left(\frac{1}{2\ell_0}\phi^2 + \frac{\ell_0}{2}|\nabla\phi|^2\right)\mathrm{d}V \tag{8}$$

where G_c is the critical Griffith-type energy release rate, which is dependent on the hydrogen coverage θ. G_c controls the free energy contribution necessary for damage accumulation to occur.

The phase-field fracture method resembles traditional continuum damage mechanics models, where the scalar damage field may be interpreted as the phase-field ϕ. Accordingly, the loss of stiffness associated with mechanical degradation of the material is characterized as a function of ϕ. This is done by means of the so-called degradation function $g(\phi)$, which relates the stored bulk energy per unit volume to the strain energy density of the undamaged solid,

$$\psi = g(\phi)\,\psi_0 = \left[(1-\phi)^2 + k\right]\psi_0 \tag{9}$$

As observed $g(\phi) = (1-\phi)^2 + k$ is a parabolic degradation function. k is a parameter chosen to be as small as possible to keep the system of equations well-conditioned [78]; a value of $k = 1\times10^{-7}$ is adopted throughout this work. Integrating over the volume of the body and adding the phase-field free energy contribution (8), one reaches the total potential energy functional of the deformation-fracture problem

$$\Psi = \int_{\Omega}\left\{\left[(1-\phi)^2 + k\right]\psi_0 + G_c(\theta)\left(\frac{1}{2\ell}\phi^2 + \frac{\ell_0}{2}|\nabla\phi|^2\right)\right\}\mathrm{d}V \tag{10}$$

The variation of (10) with respect to renders the weak form of the phase-field contribution,

$$\int_{\Omega} \left[-2\left(1-\phi\right)\delta\phi\psi_0\right] + G_c\left(\theta\right)\left(\frac{1}{2\ell_0}\phi\delta\phi + \ell_0\nabla\phi\cdot\nabla\delta\phi\right)\mathrm{d}V = 0 \tag{11}$$

and the phase-field equilibrium equation in Ω,

$$G_c\left(\theta\right)\left(\frac{1}{\ell_0}\phi - \ell_0\Delta\phi\right) - 2\left(1-\phi\right)\psi_0 = 0 \tag{12}$$

follows immediately upon making use of the product rule and Gauss' divergence theorem.

3.2. Phase-field corrosion model

The constitutive definitions for the degradation functions is grounded on the concept of the critical energy release rate dependence on the hydrogen coverage as,

$$\frac{G_c(\theta)}{G_c(0)} = 1 - \chi\theta \tag{13}$$

where $G_c(0)$ is the critical energy release rate in the absence of hydrogen and χ is the damage coefficient that weights the hydrogen-lowering of the fracture energy.

Next, the Langmuir-McLean isotherm [79] is used to compute the surface coverage from the bulk hydrogen concentration C,

$$\theta = \frac{C}{C + \exp\left(\frac{-\Delta g_b^0}{\mathcal{R}T}\right)} \tag{14}$$

with C given in units of impurity mole fraction. Here, $\mathcal{R}$ is the universal gas constant, T the temperature and Δg_b^0 is the Gibbs free energy difference between the decohered interface and the surrounding material. A value of 30 kJ/mol is assigned to Δg_b^0 based on the spectrum of experimental data available for the trapping energy at grain boundaries. Thus, the present formulation accounts for the effect of microstructural traps on cracking and can incorporate the influence on mass transport through an effective diffusion coefficient. A detailed presentation of the phase-field formulae for hydrogen-assisted cracking and fatigue including governing balance equations, energy imbalance, constitutive theory,and numerical implementation is presented elsewhere [66, 68].

3.3. A coupled phase-field corrosion-fracture model

The deformation, diffusion and phase-field fracture problems are weakly coupled. First, mechanical deformation impacts diffusion through the stress field, governing the pressure dependence of the bulk chemical potential. Secondly, mass transport affects the fracture resistance via hydrogen buildup in the fracture process zone, reducing the critical energy release rate. And thirdly, the hydrogen-sensitive phase-field degrades the strain energy density of the solid.

We solve the linearized finite element system by means of a time parametrization and an incremental-iterative scheme in conjunction with the Newton–Raphson method. The elastic displacement and the fracture problem are decoupled and solved separately as a staggered solution [77, 78]. The strategy is computationally efficient and extremely robust. A time increment sensitivity analysis is conducted. The modeling framework is implemented in the commercial finite element package ABAQUS [80] via a user element subroutine. The flowchart of the approach is depicted in Fig. 3.

4. Numerical examples

We shall now show the robustness and capabilities of the present phase-field formulation. Firstly, fracture is addressed in representative numerical examples including the uni-axial traction of a softening bar and notched square plates subjected to either uni-axial tension, pure shear, or a hydrogenous environment. Then, experimental validation of this model is given by simulating the role of crack initiation life in a compact tensile test. Next, single and double pit models are investigated to unveil the effect produced by the pit shape in the posterior crack initiation and

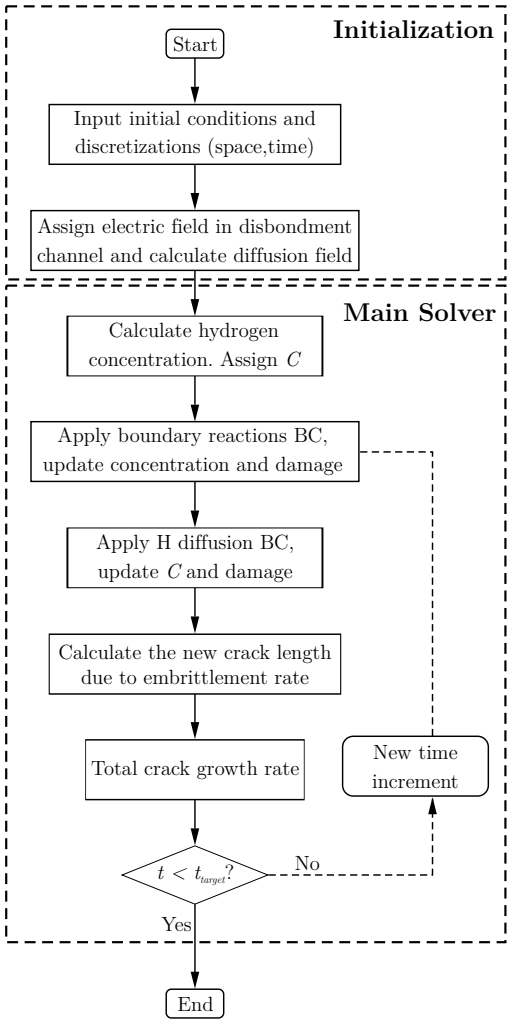

Figure 3: Flowchart of the proposed phase-field multistage model for predicting stress corrosion crack initiation life.

propagation. Finally, the most remarkable experimental validation is carried out by simulating a colony of cracks in a tensile corrosion fatigue test. The model creates pits randomly on the surface and based on a combination of density mismatch (corrosion effect) and reduction of material toughness (embrittlement effect), some of these pits are developed into multiple surface cracks.

4.1. Uni-axial traction of a softening bar

A single-edge notched tensile specimen was adopted as the first validation test. Fig. 4a shows the boundary conditions and the geometry of the specimen. The total dimension of the element is 80×10 mm in x and y directions, respectively. It has a unit out-of-plane thickness under uni-axial traction. The bottom corner nodes are constrained in both directions, whereas the top nodes are vertically stretched by a monotonically increasing displacement.

The Young's modulus of the specimen is set to $E = 210$ kN/mm^2 and the Poisson's ratio to $\nu = 0.3$. The critical energy release rate is $g_c = 5 \times 10^{-3}$ kN/mm. Two scale parameters, $\ell_0 = 0.1$ mm and $\ell_0 = 0.125$ mm respectively, are considered. The deformation is applied in $1000 \times \Delta u_y$ steps, where $\Delta u_y = 10^{-4}$ mm steps. Fig. 4b shows the crack phase-field solution at the final step. As can be observed, the localization band formed at the boundary edges. The main reason for not capturing the localization band at the interior edge is that for this simple problem the $\phi = 0$

Dirichlet condition was not imposed on the crack phase-field of the top boundary. The variable axial stress and strain result due to the tension for three different length scale parameters are presented in Fig. 4c.

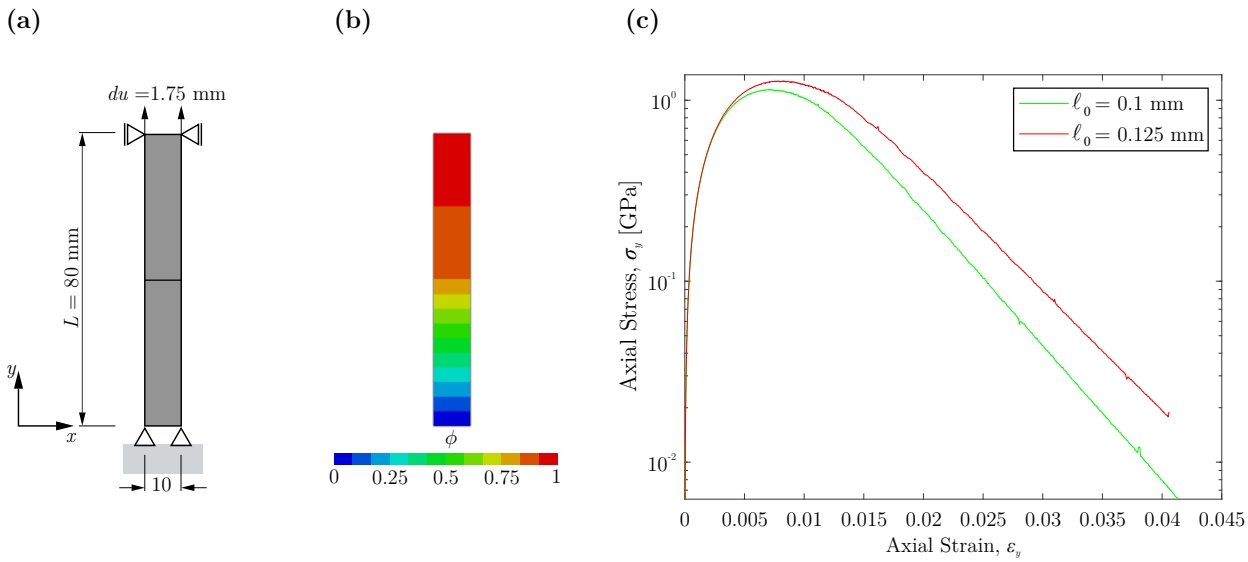

Figure 4: (a) Geometry and boundary conditions of a simple tension test with two finite elements. (b and c) Axial stress as a function of axial strain using different length scale parameters (ℓ_0) for two elements subjected to uni-axial tension.

4.2. Single-edge notched plate

The second benchmark test is concerned with a single-edge notched plate under either tensile, shear stresses, or hydrogen concentration. The geometry and the boundary conditions of the square plate of length 1 mm, with unit out-of-plane thickness, are depicted in Fig. 5a. A straight horizontal notch of length 0.5 mm is introduced at the mid-height of the left edge. The bottom edge is fixed, while the top side is moved using vertical displacements for the tension test and horizontal displacements for the shear test, respectively. The following material parameters are adopted: Young's modulus $E = 210$ kN/mm^2, Poisson's ratio to $\nu = 0.3$, and the critical energy release rate is $g_c = 2.7 \times 10^{-3}$ kN/mm. In order to relieve computational burdens, the plate is meshed with a refined zone at the expected crack propagation region, while the region away from the crack propagation zone has approximately ten times higher finite elements size. The finite element mesh has ≈22, 000 elements. The region around the crack path is refined in order to reach the maximum of $h = 0.001$ mm mesh size. Tensile loading is applied by $\Delta u = 10^{-4}$ mm for 500 steps, then $\Delta u = 10^{-5}$ mm to precisely follow the overall propagation. While the shear deformation was applied in $\Delta u = 10^{-4}$ mm for 1000 steps. Then the step size was reduced similarly to the tensile case to $\Delta u = 10^{-5}$ mm. The change in the step size is applied to be consistent with the results of Miehe et al. [77, 78].

The tension test producing brittle fracture is first discussed. Fig. 5b depicts the crack patterns (phase-field contours) at displacement $du_y = 0.09$ mm. For tension at (α=90°), the brittle crack is found to be placed horizontally. In this example, we examined the effect of the finite element size, load step, and length scale parameter. The force versus displacement response surface for this three studies is presented in Fig. 6a. One can observe a large variation in the force-displacement curve for high load rates. This is due to the unstable cracking propagation of the problem. Regarding the effect of the length scale parameters, it can be seen that the maximum reaction force value almost agrees and there is a slight deviation in the propagation period only. This is a direct consequence of the phase-field regularized approximation to the sharp crack. Contrary, the minimum mesh element $h_{\min}$ seems to affect the maximum force response only.

Regarding to shear loading conditions, the crack pattern at displacement $du_x = 0.02$ mm are shown in Fig. 5c. A curved crack path initiating with approximately 60° angle from the direction of the deformation is spotted. Similar to those presented in the literature [77, 78, 81], the crack pattern is found to nucleate at the pre-notch tip and propagates

down to the right bottom corner. The shear evolution behaviour is depicted from the predicted load versus displacement curves in Fig. 5b, which are consistent with those presented in the literature [63, 77]. Note also from the figure that the length scale affects to a minor extent the global shear responses.

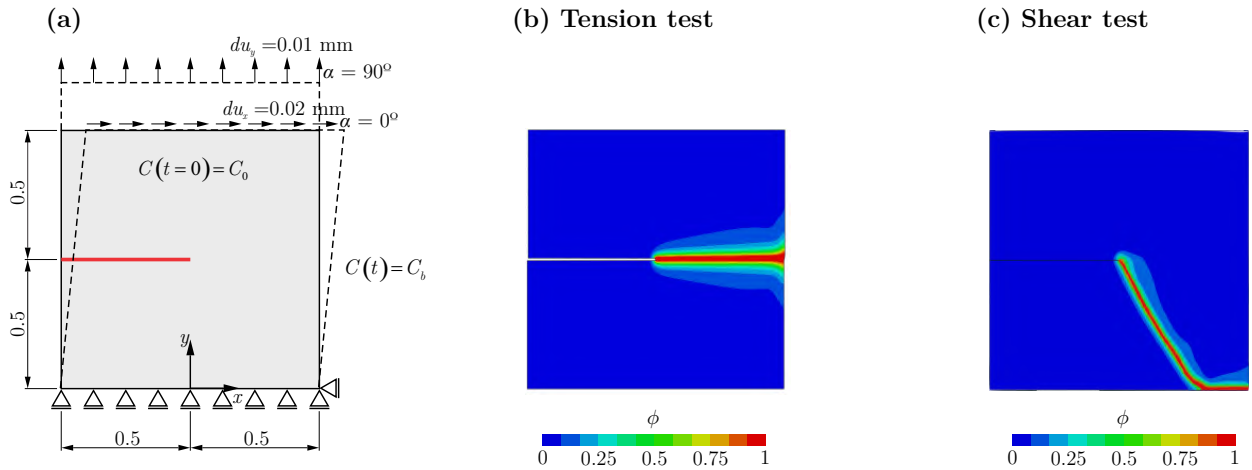

Figure 5: (a) Geometry and various cases of boundary conditions of a single edge notched specimen under either tension, pure shear, or hydrogenous environment. (b) Contours of the phase-field ϕ after rupture by tension at displacement $du_y = 0.09$ mm. (c) Contours of the phase-field ϕ after rupture by shear at displacement $du_x = 0.02$ mm.

To conclude this section, let us describe the effect of hydrogenous environment on the tensile test. To that end, an initial uniform hydrogen distribution $C(t = 0) = C_0$ is applied through outer surfaces using a Robin-type mass transport condition. This boundary condition is applied from initiation $t = 0$ start at the plate edges to model the species absorption. Simulations are carried out with a long testing time, often the time of failure t_f overpassing 2×10^6 s, which allows for hydrogen to redistribute in the fracture process zone. Fig. 6c shows the force-deflection response surface as a function of the hydrogen concentration. As observed, the model reproduces a drop of the force maximum at higher hydrogen concentrations.

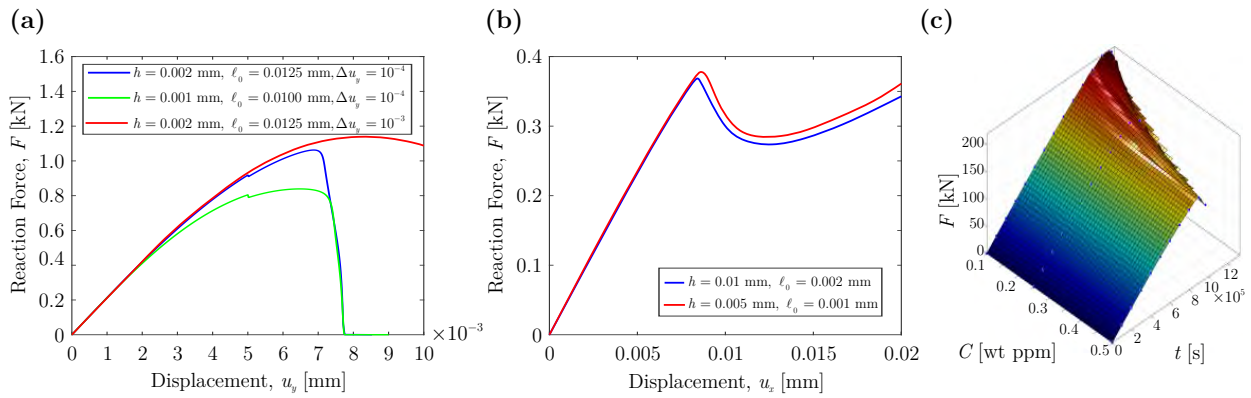

Figure 6: Various cases of load *versus* displacement curves of a single edge notched plate. (a) Study of tensile load under the effect of element size (h), displacement load rates (Δu), and length scale parameters (ℓ_0). (b) Study of shear forces considering two cases of element size (h) and length scale parameters (ℓ_0). (c) Study of the effect of hydrogen concentration for the tensile load case.

4.3. Compact tensile test in a hydrogenous environment

In this section, we use the proposed phase-field model to simulate the internal hydrogen diffusion measured during compact tensile (CT) tests performed by [20, 82] on X80 steel. In the experiment, CT specimens were subjected to

NS4 solutions with 5% and pH between 3 to 8. The NS4 solution has properties typical of those found in coating-disbonded areas of Canadian pipelines. Hydrogen diffusion into the steels around the crack tip was measured using secondary ion mass spectrometry (SIMS). Fig. 7a show the geometry, dimensions, and the mesh of the specimens according to the experiment, ASTM E 1820 Standard, and this work. The material properties related to the mechanical response are Young's modulus $E = 210$ kN/mm^2, Poisson's ratio $\nu = 0.3$, and fracture energy $G = 1,000$ J/m^2. The experiments have been conducted at room temperature and the diffusion coefficient $D = 2 \times 10^{-8}\text{m}^2/\text{s}$ proposed by [83] for a new X70/X80 type with an acicular ferrite pipeline microstructure is adopted. As per the experiment, CT specimens were loaded by a wedge with different levels of J-integral value. The length parameter is chosen to be $\ell_0 = 0.025$ mm, 5 times larger than the characteristic element length along the extended crack plane. Fig. 7b shows the predictive and measured hydrogen concentration near crack tip for applied J-integral values of 32, 102 and 136 MJ/m^2. Overall, higher applied forces induced higher hydrogen concentrations near the crack tip. Furthermore, the hydrogen accumulation peak ahead of the crack tip was captured accurately. For decreasing pH values, the peak became more pronounced. This first peak was close to the crack tip, while the second peak obtained in the experiments was located approximately 1 mm from the crack tip. The horizontal portions shown in Fig. 7b corresponded to regions of the sample where the concentration of hydrogen was equal to the bulk average value.

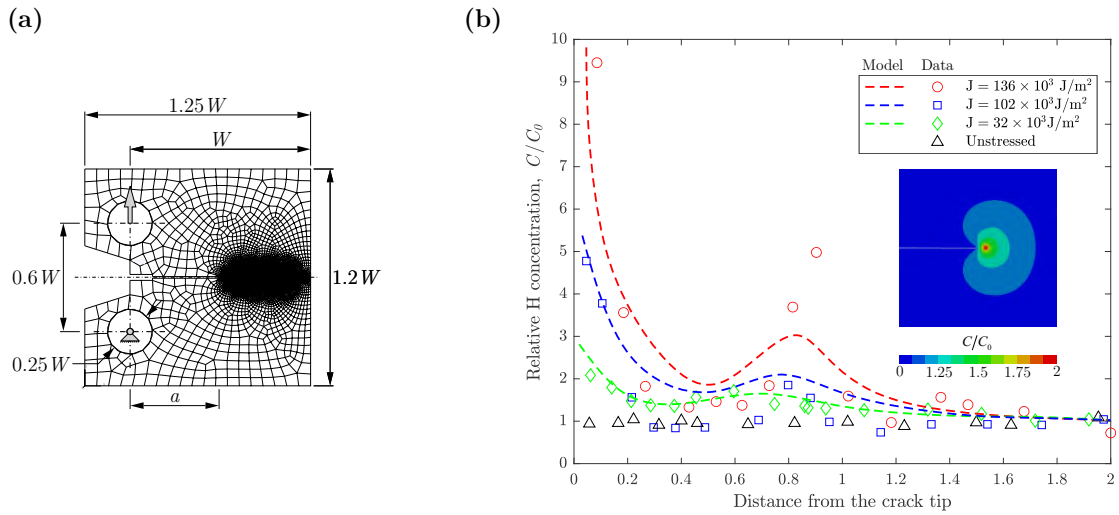

Figure 7: Compact tensile tests in a near-neutral pH environment: (a) details of the geometry and mesh of the compact tensile specimen. (b) Results of the hydrogen distribution near the crack tip for various levels of J-integral loading conditions. The inset contour plot indications of hydrogen buildup in the fracture process zone.

The second set of analyses examined the influence of increasing cathodic potential (CP) on the crack growth rate. It is known that CP increase is translated into higher hydrogen concentration around the crack tip. For example, during CT tests measured at $E_{corr} = -750$ mV$_{\text{SCE}}$, the bulk hydrogen concentration was found to be 2.4 ppm. Similarly, if a cathodic potential of -1000 mV$_{\text{SCE}}$ was applied, the hydrogen concentration increased to 4.2 ppm. Fig. 8a shows that numerical predictions qualitatively capture typical crack propagation paths. The most striking results, however, are those presented in Fig. 8b, namely, the effects of the potential on significantly increasing hydrogen content and crack growth rates. Similar observations were obtained in other tests (e.g., [84, 85]). At the top of Fig. 8b we show scanning electron microscopy (SEM) fractographs of samples that were tested at different potentials. These fractographs shed lights into the expected effects of internal HE. Depending of the applied potential, these includes the development of shear dimples at the anodic potential, -550 mV$_{\text{SCE}}$, cleavage mixed with dimples at E_{corr}, -750 mV$_{\text{SCE}}$, and areas of quasi-cleavage at the cathodic potential, -1000 mV$_{\text{SCE}}$.

4.4. Parametric pit simulations

In order to investigate the effect produced by the pit shape in the posterior crack initiation and propagation, four corrosion pits shapes were initially assumed: hemisphere, butterfly, frustum, and bullet. For all geometries, the pit

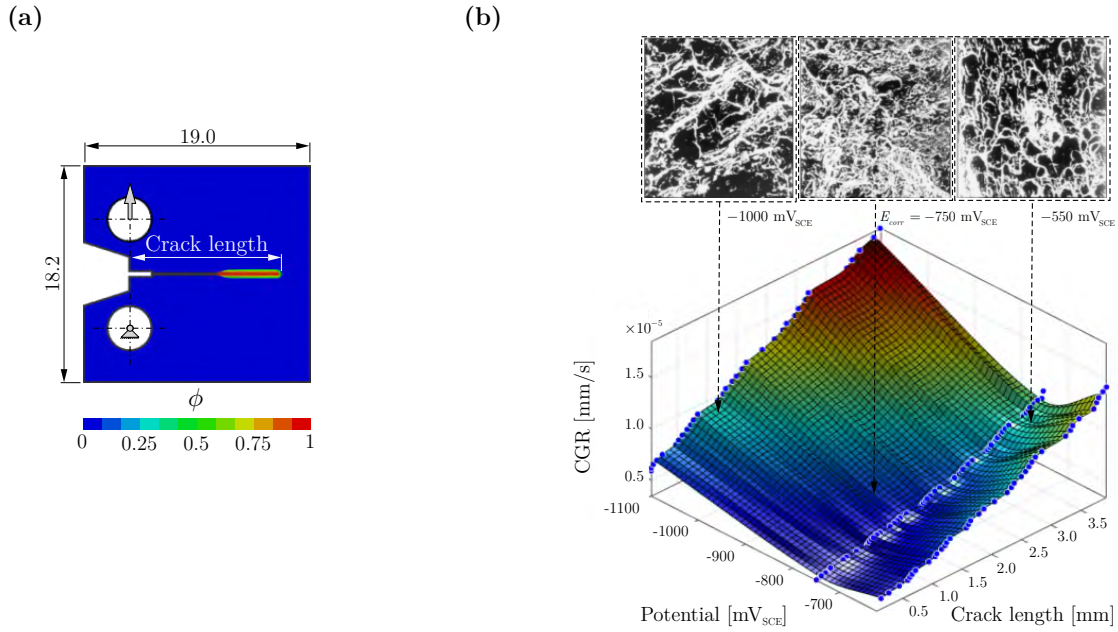

Figure 8: (a) Results from phase-field simulations of crack growth rate in X80 pipeline steel under various cathodic potential levels. Above the 3D surface are included SEM photographs for X80 steel samples tested at -550 mV$_{SCE}$, -720 mV$_{SCE}$, and -1000 mV$_{SCE}$, respectively, obtained from ([20].

aspect ratio a_p/r_p (depth over a radius of the pit on the surface) is considered in the range from 0.25 to 2.0. In this work, we consider pits within the range of 100 μm to 500 μm. To reduce the computational demands of these geometries, a quarter pit model with two planes of symmetry is developed. Boundary conditions are applied unloaded by holding translation degree of freedom at x and z directions.

As regards loading conditions, it is well-known that depending upon various factors maximum allowable hoop stress produced by the operating pressure can be set up to 80% of the specified minimum yield strength (SMYS) for a pipe steel CSA [86]. However, most pipelines operate with a hoop stress limit of 72% SMYS [7, 24]. Note that the yield strength of the pipe is usually higher than the SMYS, sometimes in the range of 10 to 30% [11, 24]. Residual stresses and local stress raisers, other than pits such as scratches and dents, can significantly increase the local effective stress in the pipe. Operating hoop stress of 72% SMYS and residual stress of 25% SMYS were used as representative maximum local hoop stress loading conditions for the majority of simulations. That is, the effective hoop stress is 97% SMYS.

First, we examined the relationship between the pit size and the surrounding domain, so that the pipe material surrounding the pit can be considered as a semi-infinite body. That is, the pit depth has to be small enough compared to the wall thickness, hence avoiding an increase of stress around the pit and unrealistic stress concentration at the pit mouth. To confirm the validity of treating the pit as if it exists in a semi-infinite body a number of simulations with different pit depths over domain sizes were carried out and the results are presented in Fig. 9a. The main results are given as stress concentration factor (SCF), which is the ratio of maximum principal stress to nominal applied stress at the root of the corrosion pit. It is observed that for pit depths less than roughly 10% of the domain dimension (e.g., wall thickness) the concentration of stress at the pit depth is independent of pit size. A characteristic corrosion pit observed in association with colony initiation in a near-neutral pH environment is seldom higher than 0.5 mm in depth [24]. Thus, based on our modeling experience, a 5 mm domain yields size-independent results and has been used in the parametric analysis.

Turning now into the effects of mesh density, the first aspect to note is that the mesh was refined in the surroundings of the pit to enhance the accuracy of stress and strain predictions. Fig. 9b presents the results of mesh convergence

analysis. The applied external stress is applied to each model with subsequent model mesh refined mesh until further refinement offered no significant change in SCFs. One can observe that the SCF converged in all models after a refined mesh with element size between 10 to 5 μm at the pit location. This means that, although the meshes were adapted to each pit's geometry, similar levels of predictive accuracy were obtained with this small element size. It is interesting to note that the 5 μm element size can be found as a typical grain size on the material scale [87]. Furthermore, the use of this characteristic length scale in FEA enabled efficient prediction of corrosion fatigue and fracture [26]. Thus, a mesh with the 5 μm element size offers sufficient precision and consistency for the purposes of this modeling and was used throughout. Fig. 9c shows the percentage change in the prediction of stress concentration factors from the previous to the current mesh and the cost associated with processing time. Although, refining the mesh to 5 μm does not provide quicker results, the expected error is less than 1%. As observed, a 50 μm element size could give reasonably good approximations while saving disc space and run time, but the 5 μm mesh is selected herein for the reasons above-mentioned.

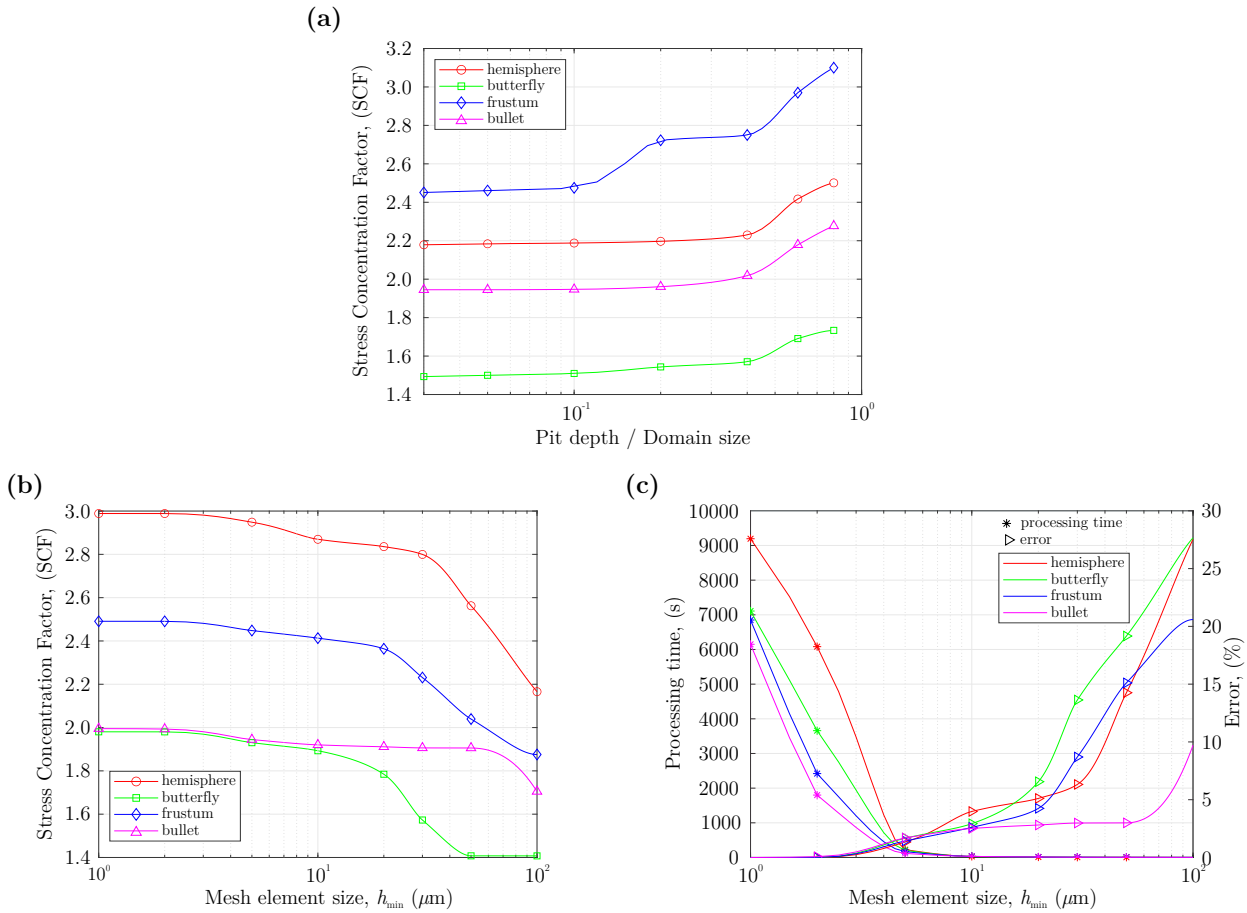

Figure 9: Effect of the domain size on developing localized mechanical stress. For all pit shapes the pit aspect ratio is $a_p/r_p = 1$. (b) Mesh convergence analyses based on stress concentration factor, pit shape, and mesh size. For all pit shapes the pit depth is 500 μm and the pit radius is 250 μm , i.e the aspect ratio is $a_p/r_p = 2$.

Since the domain and mesh density was checked, let us now present the effects of pit aspect ratio on the predicted hoop stresses for the butterfly and hemisphere pits. As depicted in Fig. 10, hoop stresses at both the pit base and mouth for these pit configurations, are increased. On other hand, as the aspect ratio increases the hoop stresses at the pit mouth reach maximum stress, which is approximately 50% of the yield strength for a 0.5 aspect ratio, but steadily decreased afterward. Another observation is that the base of hemisphere pits showed a steeper constant increase of the hoop stress with an increase in aspect ratio. This is the pit shape and location with higher stresses, so that can take

up to 70% of the available yield strength when the aspect ratio is 1.5. For all future analyses, the hemisphere pit is considered as the main pit shape.

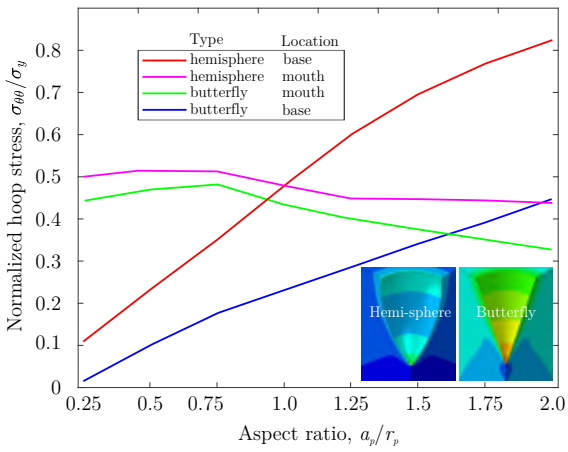

Figure 10: Effect of the pit shape in the evolution of hoop stresses. Inset figures shows stress distribution fields on the cone and hemisphere type corrosion pits.

We now assumed that highly localized stresses resulting from a density mismatch between the original material and corrosion products within the pit present a more severe threat to the nucleation of cracks. To that end, the buildup of mechanochemical stresses produced by corrosion products are modeled as density mismatch. Choi and Chudnovsky [21] defined the density mismatch as the ratio of the negative density increment $\rho_{om} - \rho_{cp}$ (where ρ_{cp} stands for the corrosion products density) over the original metal density ρ_{om}, i.e., , $\left(\rho_{om} - \rho_{cp}\right)/\rho_{cp}$. This effect is well denoted characteristic of narrow and deep (trough) pits since the released volume corrosion product is larger than the pit cavity. Furthermore, because part of corrosion products is discharged from the pit cavity, only a portion of the increased volume of corrosion products results in tensile stresses in the vicinity of the corrosion pit. In order to consider these contributing features to buildup stresses, we modeled the density mismatch as an inner displacement boundary condition based on circular von Mises distribution. That is, radial displacements were applied to all of the nodes in the fictitious region as a solution for a conventional boundary condition that applies displacement to the domain nodes near the pit surface. Fig. 11 shows a representative distribution of stress cracking in a modeled hemisphere pit with an initial depth and radius of 270 μm subjected to 97% SMYS far-field stress. We detected that the stress is localized around the bottom of the pit while the strain is localized just below the pit mouth in the pit shoulder due to the loss of the constraint at this location. Due to this singular distribution, the material yielded across the pit section with higher values on the minimum constraint region. That is, from a mechanistic point of view, this is the preferable location for crack development. From an energetic perspective, it is expected that the growth rate of embryo cracks at the pit shoulders slow down the pit growth rate. On the other hand, the influence of corrosion products on the crack trajectory can lead to the consideration of a stochastic process that results from the random fluctuation of material toughness in the vicinity of the pits.

Interesting observations can be extended by modeling the time evolution of the SCC process when two pits interact, as shown in Fig. 12a. In that case, we observe pits elliptically growing, that is with an extended direction perpendicular to the applied load direction. This localized and faster corrosion rate is a consequence of higher stress/strain concentrations in those regions. Cracking occurs from embryo cracks initiating at both pits. Recent experimental observations of cracking between two pits are also illustrated in the figure.

4.5. Simulation of tensile tests

Having explored important parameters of pit modeling, let us now shed light on the effects produced by a colony of pits developing from the smooth surface. To that end we simulated the tensile test shown in Fig. 13a. In this test, specimens (Fig. 13b) were subject to remote tension stress under fatigue conditions at various stress levels. Cyclic loading was provided with an MTS machine at a loading frequency of 0.1 Hz and a stress ratio of 0.5. The maximum

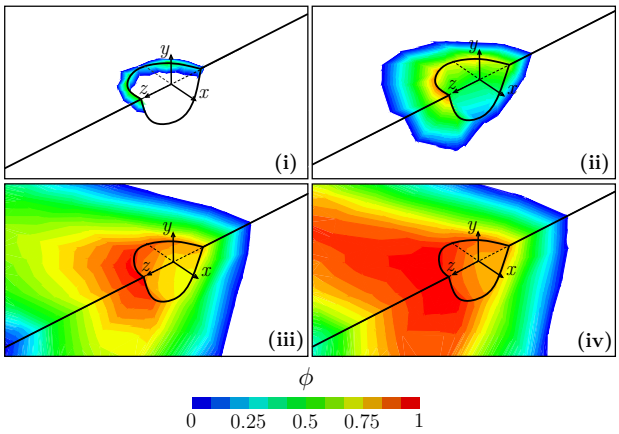

Figure 11: Crack evolution from a hemisphere pit with depth and radius of 270 μm subjected to 97% SMYS far-field stress.

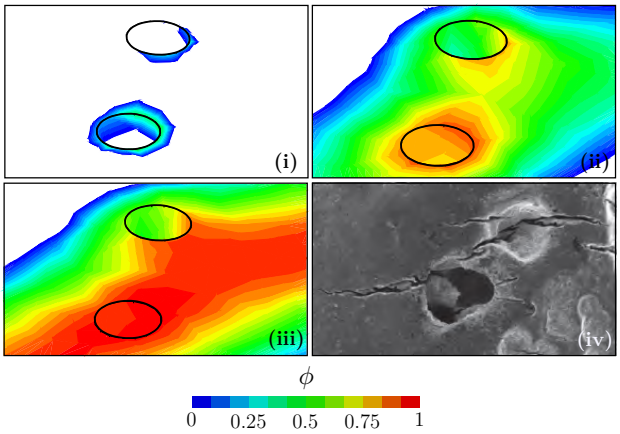

Figure 12: Prediction of pit-to-crack transition for two growing pits. (iv) is shown for comparison of pits and embryo cracks obtained from 3D imaging photographs from pit near the pit mouth using XCT [88].

applied load was selected to satisfy the maximum local stress $\sigma_{\text{max,local}}$ at the middle cross section does not exceed $1.05 \cdot$ SMYS. During the test, specimens are contained fully immersed in a chamber and put into contact with the NS4 near-neutral pH solution. The solution is considered under deaerated conditions and with a constant pH of 6.5 pH points. For the applied displacement loading, gripping is placed outside the chamber to avoid spurious galvanic coupling. SCC growth is measured in situ with an optical microscope with the acetate replica technique. Stress intensity factor range K rises through K_{th} toward ductile fracture in each test. This provides for each specimen a full range of da/dt vs. ΔK data. A total of 25 tensile specimens' measurements were obtained considering the values of time to failure (ttf) reported. From these measurements, 13 measurements were reported for the original surface while 37 for the ground surface. These data measurements represent approximately 5,000 days of laboratory exposure.

In the model, we considered that the bottom edge of the specimen's gauge is fixed and the top edge is loaded with prescribed tensile stresses (see Fig. 13c). The following material properties are assumed: Young's modulus $E = 210$ kN/mm^2, Poisson's ratio $\nu = 0.3$, density $\rho = 7.8$ g$\big/$cm^3, damage coefficient $\mathcal{X} = 0.89$, and the critical energy release rate is $g_c = 2.7 \times 10^{-3}$ kN/mm. We also adopted a partial molar volume of $\bar{V}_{\text{H}} = 2000$ mm$^3\big/$mol and a normal diffusivity of $D = 2 \times 10^{-8}$ m$^2\big/$s. We consider the phase-field length parameter ℓ_0 as four times mesh units h, which corresponds to a range between 2 and 16 μm, and presented its effect in each finite element.

The simulation of virtual domains of the colony initiation stage with a fixed intensity level of pitting is carried out and presented next. To that end, an initial number of randomly located pits are nucleated in the gauge's area. This aims

to capture the most important feature of actual domains so that actual and virtual domains have the same statistical characteristics in terms of random distribution of pits and crack-pit at initiation (i.e., nucleation). The modeling and prediction of surface pitting behavior require the information of pit location and initial pit depth distribution within a domain of the colony. We considered that the location of a number of random corrosion pits is given by a Poisson distribution. The initial distribution of stable pit depths is also assumed to be defined by a Poisson distribution of 300 μm mean depth and standard deviation to mean ratio of 0.18.

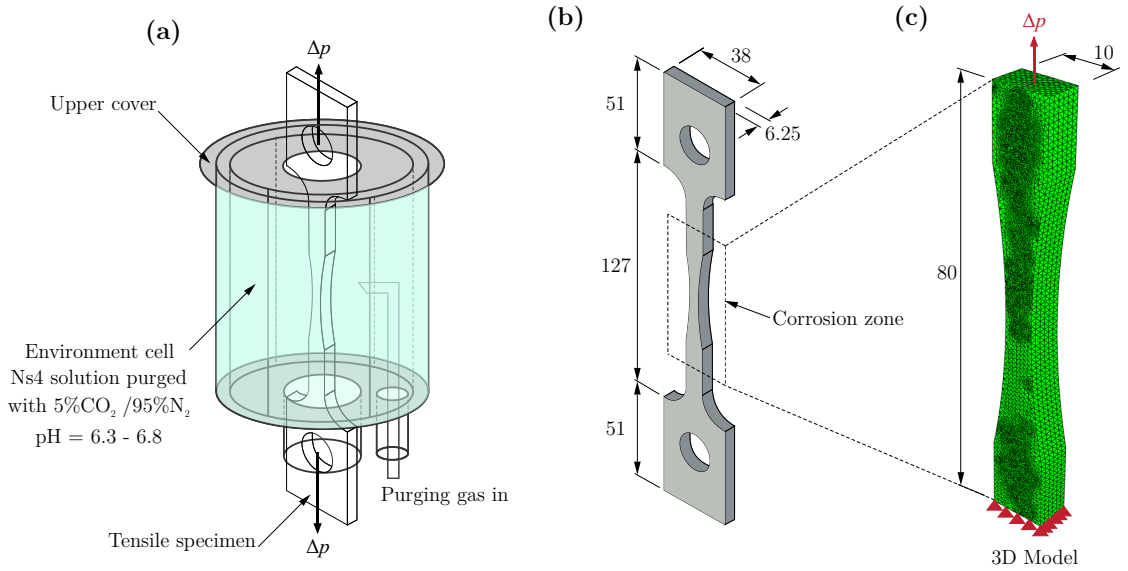

Figure 13: (a) Schematic drawing of the corrosion test cell with specimen, (b) geometry and dimensions of the specimen, (c) 3D FE model including dimensions, details of the mesh, and boundary conditions.

The first set of analyses examined the impact of pitting distribution on times of failure during tests. Fifty simulations were used for each applied stress level, with Monte Carlo simulation of a Poisson field of corrosion pits and crack initiation from some of those pits. Material, residual stress, and electrode potential variability were not modeled. Note that although the pit density was not specified in the test, analyses with 50 pits appeared to generate a similar number of cracks as those reported experimentally. Observation of a typical modeled specimen until failure is displayed in Fig. 14. After the first crack nucleation events of the colony, a period of short crack propagation starts. This is a period where individual crack growth occurs driven by mechanical stresses and electrochemical processes. Fig. 14a shows that, as the crack propagates from embryo cracks to individual short cracks, those pits appeared to discharge stress concentration to the crack tip. Significant crack interaction with conventional features of cracks in colonies, such as irregularly crack propagation, zones of stress concentration and zones of stress relaxation, crack tip interaction with coalescence (i.e., amplification) or without coalescence (i.e., shielding), and areas of small plastically deformed ligaments, were all simulated accordingly. The level of interaction observed reveals their high correlation to the relative position and time of their initiation. It is observed that neighboring cracks had their tip curved as they come close. However, the complex process and the crack interaction intensity depend largely on the stage of growth, and hence various mechano-electro-chemical aspects that may be changing the system behavior should not be disregarded. The general interaction between the cracks, with or without coalescence, seems to be more disturbed during the staring propagation process. First initiated long cracks can easily arrest later initiated small cracks by the shielding effect. On the other hand, the larger crack propagates more rapidly by the amplification effect. These are the so-called active cracks. As the distance between neighboring cracks is reduced the crack interaction increases and eventually a critical size cluster of cracks is formed and leads to failure.

Turning now into the lifetime prediction, the model was remarkably good at predicting the overall effect of crack-in-colonies and the mean applied stress range on the SCC resistance. As expected, the increase of applied mean loads shows an effect on the crack interaction, and hence it affects the maximum local stress distribution of the specimen.

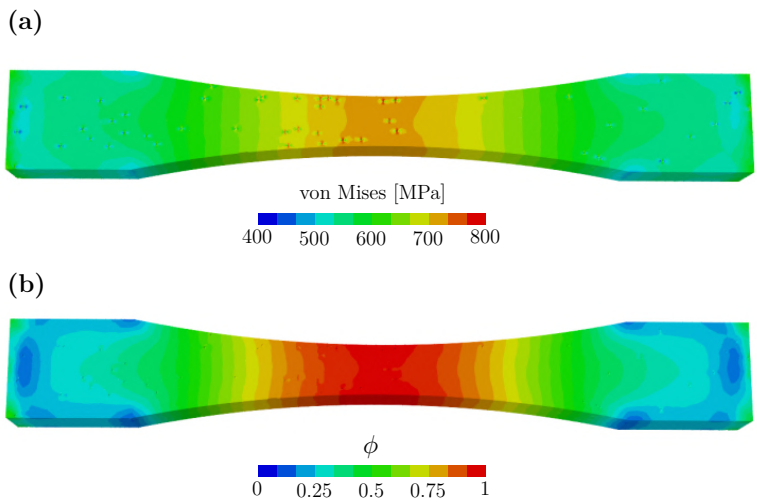

Figure 14: Numerical simulation of tensile tests showing: (a) the propagation of the von Mises stress field during crack initiation stage for an applied stress $\sigma_{\text{max,local}} = 1.05 \cdot \text{SMYS}$ and (b) phase-field variable.

As shown in Fig. 15a, for the lower stressing conditions the fatigue life of test specimens is four times larger than the higher stress conditions. The probability density function of the simulated times to failure is reported in Fig. 15b. The solid line corresponds to the best fit normal distribution and the dashed line to the best fit kernel density estimation. Significant variation for times to failure observed justifies the need of performing the proposed probabilistic analysis of a pit colony.

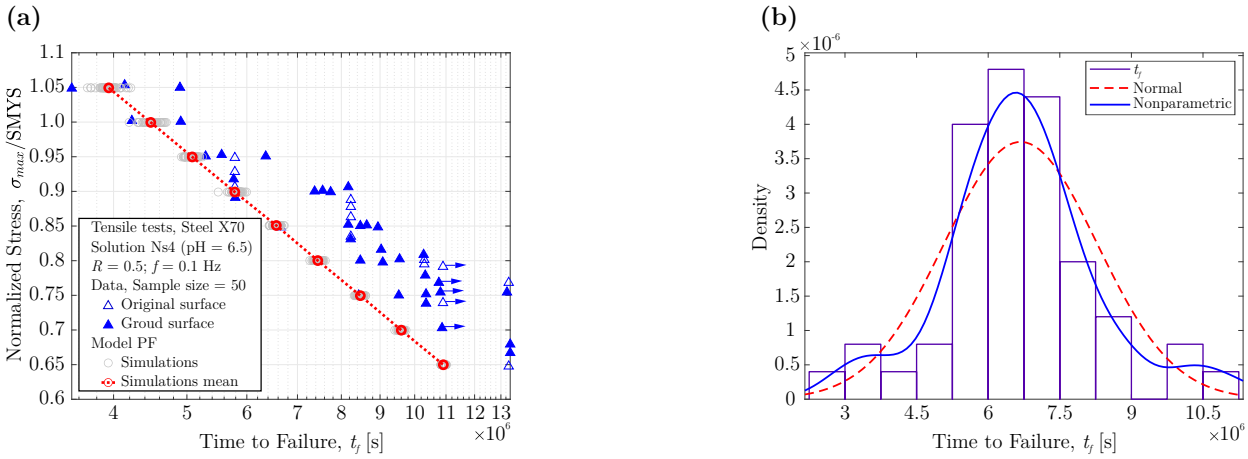

Figure 15: (a) Predicted versus observed time to failure at different remote stresses of X70 steel in NS4 and (b) histogram of the estimated time to failure. The depth of the surface crack was Monte Carlo selected as the random variable from hypothetical-lognormal distribution with a mean depth of 300 μm and standard deviation/mean of 0.18.

To conclude this section, Fig. 16 presents the obtained average crack growth rate for each stressing condition. As observed, crack growth rates are essentially independent of the applied stress level. Furthermore, it is seen that the crack growth rate is very low and in the order of 10^{-9} to 10^{-8} mm/s. Interestingly, a large dispersion in the prediction was observed for the higher applied stress. At such stress levels, the crack growth rates appeared to be highly sensitive to plasticity straining effects. As the crack initiation has not been directly calculated, the crack propagation rate predicted in this work should be related to crack behavior in colonies only.

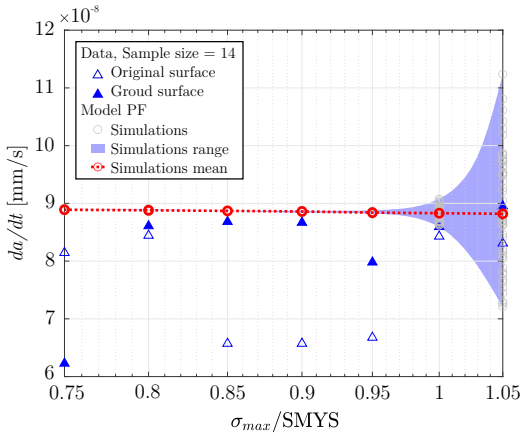

Figure 16: Crack growth rate distribution for independent cracks and crack clusters in the colony assessed at various load levels.

5. Concluding remarks

A comprehensive phase-field approach has been proposed to examine the mechano-chemical corrosion behavior of the initiation of stress corrosion crack colonies of buried pipelines in contact with a near-neutral pH environment. The main advantages of the model lie in its capability to reproduce the pit-to-crack transition by means of unrestricted evolution of the corrosion front and the embedded heterogeneities in the corrosion damage layer. Phase-field simulations of a number of interesting problems were conducted to understand the relation between pit depth and surface-breaking cracks and the accuracy of the present phase-field formulation for hydrogen embrittlement. The most interesting validation model consisted of crack-in-colonies originating from pits in X70 steel samples subjected to tensile constant amplitude corrosion fatigue tests. It was found that intensification of interactions caused a reduction in both the number of cracks and the mean crack growth rate. It was shown that the mouth of the pit is the preferred crack nucleation site due to localized strain, however, competition between locations for crack initiation exists due to the aggressiveness of the environment and straining produced by corrosion products. Further works are required to account for the effects of corrosion kinetics in discrete microstructural and microchemical features on a much-refined scale, as they are important parameters for determining actual crack growth rates. It is also expected that the proposed methodology can be progressively extended at a larger scale to simulate SCC on pipelines under service conditions including a range of surface conditions such as the effect of residual stress on crack dormancy.

Acknowledgement

The authors acknowledge the financial support through the Natural Sciences an Engineering Research Council of Canada (RGPIN-2019-05584) under the Discovery Grant programs, MITACS Accelerate and the BC Oil and Gas Research and Innovation Society (BC OGRIS).

References

[1] R. N. Parkins, W. K. Blanchard Jr, B. S. Delanty, Transgranular Stress Corrosion Cracking of High-Pressure Pipelines in Contact with Solutions of Near Neutral pH, Corrosion Engineering 50 (1994) 394–408.

[2] NEB, Stress Corrosion Cracking on Canadian Oil and Gas Pipelines, Report of the Inquiry, MH-2-95, Technical Report, National Energy Board, Calgary, Alberta, Canada, 1996.

[3] M. Baker Jr., Stress Corrosion Cracking Study, Technical Report, Department of Transportation, Research and Special Programs Administration, Denver, CO, US, 2005.

[4] W. Zheng, M. Elboujdaini, R. W. Revie, Stress corrosion cracking in pipelines, in: V. S. Raja, T. Shoji (Eds.), Stress corrosion cracking: Theory and practice, 2011, pp. 749–771. doi:10.1533/9780857093769.4.749.

[5] C. Guerre, M. Frégonèse, Q. Auzoux, I. Aubert, C. Duhamel, 14 - Stress Corrosion Crack Propagation, in: C. Blanc, I. Aubert (Eds.), Mechanics - Microstructure - Corrosion Coupling, Elsevier, 2019, pp. 313–338. URL: http://www.sciencedirect.com/science/article/pii/B9781785483097500144. doi:https://doi.org/10.1016/B978-1-78548-309-7.50014-4.

[6] CEPA, Stress Corrosion Cracking Recommended Practices, Technical Report December, Canadian Energy Pipeline Association, Calgary, Alberta, Canada, 2007.
[7] Y. F. Cheng, Stress Corrosion Cracking of Pipelines, John Wiley and Sons, Inc., Hoboken, New Jersey, USA, 2013.
[8] CEPA, CEPA Recommended Practices for Managing Near-neutral pH Stress Corrosion Cracking, Technical Report, Canadian Energy Pipeline Association (CEPA), Calgary, Alberta, Canada, 2015.
[9] B. Delanty, J. O'Beirne, Major field study compares pipeline SCC with coatings, Oil and Gas Journal 90 (1992) 39–44.
[10] W. Chen, R. Kania, R. Worthingham, G. V. Boven, Transgranular crack growth in the pipeline steels exposed to near-neutral pH soil aqueous solutions: The role of hydrogen, Acta Materialia 57 (2009) 6200–6214. doi:10.1016/j.actamat.2009.08.047.
[11] J. Zhao, W. Chen, M. Yu, K. Chevil, R. E. G. Eadie, G. V. A. N. Boven, R. Kania, J. Been, S. Keane, Crack Growth Modeling and Life Prediction of Pipeline Steels Exposed to Near-Neutral pH Environments: Dissolution Crack Growth and Occurrence of Crack Dormancy in Stage I, Metallurgical and Materials Transactions A 48 (2017) 1629–1640. doi:10.1007/s11661-016-3951-3.
[12] W. Chen, F. King, E. Vokes, Characteristics of near-neutral-pH stress corrosion cracks in an X-65 pipeline, Corrosion 58 (2002) 267–275. doi:10.5006/1.3279878.
[13] R. N. Parkins, P. M. Singh, Stress corrosion crack coalescence, Corrosion 46 (1990) 485–499. doi:10.5006/1.3585136.
[14] W. Chen, S. H. Wang, R. Chu, F. King, T. R. Jack, R. R. Fessler, Effect of precyclic loading on stress-corrosion-cracking initiation in an X-65 pipeline steel exposed to near-neutral pH soil environment, Metallurgical and Materials Transactions A: Physical Metallurgy and Materials Science 34 A (2003) 2601–2608. doi:10.1007/s11661-003-0019-y.
[15] J. A. Beavers, W. V. Harper, Stress corrosion cracking prediction model, in: Corrosion, 4189, NACE, Houston, TX, US, 2004, pp. 1–19.
[16] J. Kang, W. Zheng, D. Bibby, B. S. Amirkhiz, J. Li, Initiation of Stress Corrosion Cracks in X80 and X100 Pipe Steels in Near-Neutral pH Environment, Journal of Materials Engineering and Performance (2015). doi:10.1007/s11665-015-1822-5.
[17] G. S. Frankel, Pitting Corrosion of Metals, Journal of The Electrochemical Society 145 (1998) 2186. doi:10.1149/1.1838615.
[18] G. S. Frankel, T. Li, J. R. Scully, Perspective—Localized Corrosion: Passive Film Breakdown vs Pit Growth Stability, Journal of The Electrochemical Society 164 (2017) C180–C181. doi:10.1149/2.1381704jes.
[19] A. Turnbull, D. A. Horner, B. J. Connolly, Challenges in modelling the evolution of stress corrosion cracks from pits, Engineering Fracture Mechanics 76 (2009) 633–640. doi:10.1016/j.engfracmech.2008.09.004.
[20] B. Gu, W. Yu, J. Luo, X. Mao, Transgranular stress corrosion cracking of X-80 and X-52 pipeline steels in dilute aqueous solution with near-neutral pH, Corrosion 55 (1999) 312–318. doi:10.5006/1.3283993.
[21] B. H. Choi, A. Chudnovsky, Observation and modeling of stress corrosion cracking in high pressure gas pipe steel, Metallurgical and Materials Transactions A: Physical Metallurgy and Materials Science 42 (2011) 383–395. doi:10.1007/s11661-010-0384-2.
[22] A. Turnbull, L. Wright, L. Crocker, New insight into the pit-to-crack transition from finite element analysis of the stress and strain distribution around a corrosion pit, Corrosion Science 52 (2010) 1492–1498. doi:10.1016/j.corsci.2009.12.004.
[23] B. T. Lu, J. L. Luo, Crack initiation and early propagation of X70 steel in simulated near-neutral pH groundwater, Corrosion 62 (2006) 723–731. doi:10.5006/1.3278297.
[24] L. Wall, A Study of Hydrogen Enrichment at Pits and Other Surface Discontinuities in Mild Steel and the Contribution to Near-Neutral pH Stress Corrosion Cracking, Ph.d. thesis, University of Alberta, 2007.
[25] J. Zhao, W. Chen, M. Yu, K. Chevil, R. Eadie, J. Been, G. Van Boven, R. Kania, S. Keane, Crack Growth Modeling and Life Prediction of Pipeline Steels Exposed to Near-Neutral pH Environments: Stage II Crack Growth and Overall Life Prediction, Metallurgical and Materials Transactions A: Physical Metallurgy and Materials Science 48 (2017) 1641–1652. doi:10.1007/s11661-016-3939-z.
[26] E. R. Martínez, S. Tesfamariam, Multiphysics modeling of environment assisted cracking of buried pipelines in contact with solutions of near-neutral pH, International Journal of Pressure Vessels and Piping 196 (2022).
[27] F. P. Ford, Quantitative prediction of environmentally assisted cracking, Corrosion Science 52 (1996) 375–395.
[28] A. Turnbull, Modelling of environment assisted cracking, Corrosion S 34 (1993) 921–960. doi:0010-938X/93.
[29] B. Zhang, J. Fan, Y. Gogotsi, A. Chudnovsky, A. Teitsma, Theoretical and experimental study of stress corrosion cracking of pipeline steel in near neutral pH environmnet, in: 2000 International Pipeline Conference, ASME, 2000, pp. 1013–1020.
[30] P. Shi, S. Mahadevan, Damage tolerance approach for probabilistic pitting corrosion fatigue life prediction, Engineering Fracture Mechanics 68 (2001) 1493–1507. doi:10.1016/S0013-7944(01)00041-8.
[31] Y. Katano, K. Miyata, H. Shimizu, T. Isogai, Predictive model for pit growth on underground pipes, Corrosion 59 (2003) 155–161. doi:10.5006/1.3277545.
[32] A. Valor, F. Caleyo, L. Alfonso, D. Rivas, J. M. Hallen, Stochastic modeling of pitting corrosion: A new model for initiation and growth of multiple corrosion pits, Corrosion Science 49 (2007) 559–579. doi:10.1016/j.corsci.2006.05.049.
[33] B. Sudret, Uncertainty propagation and sensitivity analysis in mechanical models. Contributions to structural reliability and stochastic spectral methods, Technical Report, Université Blaise Pascal - Clermont II, Clermont-Ferrand, 2007.
[34] F. Caleyo, J. C. Velázquez, A. Valor, J. M. Hallen, Probability distribution of pitting corrosion depth and rate in underground pipelines: A Monte Carlo study, Corrosion Science 51 (2009) 1925–1934. doi:https://doi.org/10.1016/j.corsci.2009.05.019.
[35] J. C. Velázquez, F. Caleyo, A. Valor, J. M. Hallen, Predictive model for pitting corrosion in buried oil and gas pipelines, Corrosion 65 (2009) 332–342. doi:10.5006/1.3319138.
[36] W. Zhou, System reliability of corroding pipelines, International Journal of Pressure Vessels and Piping 87 (2010) 587–595. doi:10.1016/j.ijpvp.2010.07.011.
[37] N. Balekelayi, S. Tesfamariam, External corrosion pitting depth prediction using Bayesian spectral analysis on bare oil and gas pipelines, International Journal of Pressure Vessels and Piping 188 (2020) 104224. doi:10.1016/j.ijpvp.2020.104224.
[38] K. F. Tee, K. Pesinis, Bayesian Updating and Reliability Analysis for High-pH Stress Corrosion Cracking in Gas Pipelines, J. Eng. Mech. 146 (2020) 1–11. doi:10.1061/(ASCE)EM.1943-7889.0001803.
[39] F. Caleyo, J. C. Velázquez, A. Valor, J. M. Hallen, Markov chain modelling of pitting corrosion in underground pipelines, Corrosion Science 51 (2009) 2197–2207. doi:10.1016/j.corsci.2009.06.014.
[40] A. Valor, F. Caleyo, L. Alfonso, J. C. Velázquez, J. M. Hallen, Markov chain models for the stochastic modeling of pitting corrosion,

Mathematical Problems in Engineering 2013 (2013) 108386. doi:10.1155/2013/108386.
[41] F. Bazán, A. Beck, Stochastic process corrosion growth models for pipeline reliability, Corrosion Science 74 (2013) 50–58. doi:10.1016/j.corsci.2013.04.011.
[42] B. Gu, J. Luo, X. Mao, Hydrogen-facilitated anodic dissolution-type stress corrosion cracking of pipeline steels in near-neutral pH solution, Corrosion 55 (1999) 96–106. doi:10.5006/1.3283971.
[43] B. T. Lu, Crack growth model for pipeline steels exposed to near-neutral pH groundwater, Fatigue and Fracture of Engineering Materials and Structures 36 (2013) 660–669. doi:10.1111/ffe.12033.
[44] S. Scheiner, C. Hellmich, Finite Volume model for diffusion- and activation-controlled pitting corrosion of stainless steel, Computer Methods in Applied Mechanics and Engineering 198 (2009) 2898–2910. doi:10.1016/j.cma.2009.04.012.
[45] R. Duddu, Numerical modeling of corrosion pit propagation using the combined extended finite element and level set method, Computational Mechanics 54 (2014) 613–627. doi:10.1007/s00466-014-1010-8.
[46] E. R. Martínez, S. Chakraborty, S. Tesfamariam, Machine learning assisted stochastic-XFEM for stochastic crack propagation and reliability analysis, Theoretical and Applied Fracture Mechanics 112 (2021) 102882. URL: https://doi.org/10.1016/j.tafmec.2020.102882. doi:10.1016/j.tafmec.2020.102882.
[47] Y. Liang, P. Sofronis, Toward a phenomenological description of hydrogen-induced decohesion at particle/matrix interfaces, Journal of the Mechanics and Physics of Solids 51 (2003) 1509–1531. doi:10.1016/S0022-5096(03)00052-8.
[48] D. Ahn, P. Sofronis, R. Dodds Jr, Modeling of hydrogen-assisted ductile crack propagation in metals and alloys, International Journal of Fracture 145 (2007) 135–157. doi:10.1007/s10704-007-9112-3.
[49] B. Malki, B. Baroux, Computer simulation of the corrosion pit growth, Corrosion Science 47 (2005) 171–182. doi:10.1016/j.corsci.2004.05.004.
[50] Z. Chen, F. Bobaru, Peridynamic modeling of pitting corrosion damage, Journal of the Mechanics and Physics of Solids 78 (2015) 352–381. doi:10.1016/j.jmps.2015.02.015.
[51] Z. Chen, S. Jafarzadeh, J. Zhao, F. Bobaru, A coupled mechano-chemical peridynamic model for pit-to-crack transition in stress-corrosion cracking, Journal of the Mechanics and Physics of Solids 146 (2021) 104203. doi:10.1016/j.jmps.2020.104203.
[52] S. Jafarzadeh, Z. Chen, F. Bobaru, Computational modeling of pitting corrosion, Corrosion Reviews 37 (2019) 419–439. doi:10.1515/corrrev-2019-0049.
[53] A. Traidia, E. Chatzidouros, M. Jouiad, Review of hydrogen-assisted cracking models for application to service lifetime prediction and challenges in the oil and gas industry, Corrosion Reviews 36 (2018) 323–347. doi:10.1515/corrrev-2017-0079.
[54] N. O. Larrosa, R. Akid, R. A. Ainsworth, Corrosion-fatigue: a review of damage tolerance models, International Materials Reviews 63 (2018) 283–308. doi:10.1080/09506608.2017.1375644.
[55] E. Martínez-Pañeda, S. Del Busto, C. F. Niordson, C. Betegón, Strain gradient plasticity modeling of hydrogen diffusion to the crack tip, International Journal of Hydrogen Energy 41 (2016) 10265–10274. doi:10.1016/j.ijhydene.2016.05.014.
[56] K. Saito, J. Kuniya, Mechanochemical model to predict stress corrosion crack growth of stainless steel in high temperature water, Corrosion Science 43 (2001) 1751–1766. doi:10.1016/S0010-938X(00)00173-6.
[57] G. Qin, Y. F. Cheng, Modeling of mechano-electrochemical interaction at a corrosion defect on a suspended gas pipeline and the failure pressure prediction, Thin-Walled Structures 160 (2021). doi:10.1016/j.tws.2020.107404.
[58] A. A. Wheeler, B. T. Murray, R. J. Schaefer, Computation of dendrites using a phase field model, Physica D: Nonlinear Phenomena 66 (1993) 243–262. doi:https://doi.org/10.1016/0167-2789(93)90242-S.
[59] J. A. Warren, W. J. Boettinger, Prediction of dendritic growth and microsegregation patterns in a binary alloy using the phase-field method, Acta Metallurgica Et Materialia 43 (1995) 689–703. doi:10.1016/0956-7151(94)00285-P.
[60] A. Karma, W.-J. Rappel, Phase-field method for computationally efficient modeling of solidification with arbitrary interface kinetics, Phys. Rev. E 53 (1996) R3017—-R3020. doi:10.1103/PhysRevE.53.R3017.
[61] C. Beckermann, H.-J. Diepers, I. Steinbach, A. Karma, X. Tong, Modeling melt convection in phase-field simulations of solidification, Journal of Computational Physics 154 (1999) 468–496. doi:https://doi.org/10.1006/jcph.1999.6323.
[62] Q. Chen, N. Ma, K. Wu, Y. Wang, Quantitative phase field modeling of diffusion-controlled precipitate growth and dissolution in Ti-Al-V, Scripta Materialia 50 (2004) 471–476. doi:10.1016/j.scriptamat.2003.10.032.
[63] M. Ambati, T. Gerasimov, L. De Lorenzis, A review on phase-field models of brittle fracture and a new fast hybrid formulation, Computational Mechanics 55 (2015) 383–405. doi:10.1007/s00466-014-1109-y.
[64] S. Biner, Programming Phase-Field Modeling, Springer International Publishing, 2017. doi:10.1007/978-3-319-41196-5.
[65] J. Y. Wu, V. P. Nguyen, C. T. Nguyen, D. Sutula, S. Sinaie, S. P. Bordas, Phase-field modeling of fracture, in: Advances in Applied Mechanics, volume 53, 2020, pp. 1–183. doi:10.1016/bs.aams.2019.08.001.
[66] E. Martínez-Pañeda, A. Golahmar, C. F. Niordson, A phase field formulation for hydrogen assisted cracking, Computer Methods in Applied Mechanics and Engineering 342 (2018) 742–761. doi:10.1016/j.cma.2018.07.021.
[67] J. Y. Wu, T. K. Mandal, V. P. Nguyen, A phase-field regularized cohesive zone model for hydrogen assisted cracking, Computer Methods in Applied Mechanics and Engineering 358 (2020) 112614.
[68] A. Golahmar, P. K. Kristensen, C. F. Niordson, E. Martínez-Pañeda, A phase field model for hydrogen-assisted fatigue, International Journal of Fatigue 154 (2022) 106521. doi:10.1016/j.ijfatigue.2021.106521.
[69] P. Sthle, E. Hansen, Phase field modelling of stress corrosion, Engineering Failure Analysis 47 (2015) 241–251. doi:10.1016/j.engfailanal.2014.07.025.
[70] W. Mai, S. Soghrati, R. G. Buchheit, A phase field model for simulating the pitting corrosion, Corrosion Science 110 (2016) 157–166. doi:10.1016/j.corsci.2016.04.001.
[71] W. Mai, S. Soghrati, A phase field model for simulating the stress corrosion cracking initiated from pits, Corrosion Science 125 (2017) 87–98. doi:10.1016/j.corsci.2017.06.006.
[72] T. T. Nguyen, J. Réthoré, M. C. Baietto, J. Bolivar, M. Fregonese, S. P. Bordas, Modeling of inter- and transgranular stress corrosion crack propagation in polycrystalline material by using phase field method, Journal of the Mechanical Behavior of Materials 26 (2017) 181–191.

doi:10.1515/jmbm-2017-0024.

[73] T. T. Nguyen, J. Bolivar, J. Réthoré, M. C. Baietto, M. Fregonese, A phase field method for modeling stress corrosion crack propagation in a nickel base alloy, International Journal of Solids and Structures 112 (2017) 65–82. doi:10.1016/j.ijsolstr.2017.02.019.

[74] T. T. Nguyen, J. Bolivar, Y. Shi, J. Réthoré, A. King, M. Fregonese, J. Adrien, J.-Y. Buffiere, M.-C. Baietto, A phase field method for modeling anodic dissolution induced stress corrosion crack propagation, Corrosion Science 132 (2018) 146–160. doi:https://doi.org/10.1016/j.corsci.2017.12.027.

[75] C. Cui, R. Ma, E. Martínez-Pañeda, A phase field formulation for dissolution-driven stress corrosion cracking, Journal of the Mechanics and Physics of Solids 147 (2021) 104254. doi:10.1016/j.jmps.2020.104254.

[76] S. G. Kim, W. T. Kim, T. Suzuki, Phase-field model for binary alloys, Phys. Rev. E 60 (1999) 7186–7197. doi:10.1103/PhysRevE.60.7186.

[77] C. Miehe, F. Welschinger, M. Hofacker, Thermodynamically consistent phase-field models of fracture: Variational principles and multi-field FE implementations, International Journal for Numerical Methods in Engineering 83 (2010) 1273–1311. doi:10.1002/nme.2861.

[78] C. Miehe, M. Hofacker, F. Welschinger, A phase field model for rate-independent crack propagation: Robust algorithmic implementation based on operator splits, Computer Methods in Applied Mechanics and Engineering 199 (2010) 2765–2778. doi:10.1016/J.CMA.2010.04.011.

[79] H. E.D., S. M.P., The theory of grain boundary segregation in terms of surface adsorption analogues, Metall Trans A 8 A (1977) 1363 – 1371. doi:10.1007/BF02642850.

[80] D. Systèmes, Abaqus 6.14 Online Documentation, 2014.

[81] G. A. Francfort, B. Bourdin, J. J. Marigo, The variational approach to fracture, Journal of Elasticity 91 (2008) 5–148. doi:10.1007/s10659-007-9107-3.

[82] S. Mao, M. Li, Mechanics and thermodynamics on the stress and hydrogen interaction in crack tip stress corrosion: experiment and theory, J. Mech. Phys. Solids 46 (1998) 1125–1137. doi:0022-5096/98.

[83] M. Dadfarnia, B. P. Somerday, P. Sofronis, I. M. Robertson, D. Stalheim, Interaction of hydrogen transport and material elastoplasticity in pipeline steels, Journal of Pressure Vessel Technology 131 (2009) 1–13. doi:10.1115/1.3027497.

[84] Z. Y. Cui, Z. Y. Liu, X. Z. Wang, Q. Li, C. W. Du, X. G. Li, W. Zhang, Crack growth behaviour and crack tip chemistry of X70 pipeline steel in near-neutral pH environment, Corrosion Engineering Science and Technology 51 (2016) 352–357. doi:10.1080/1478422X.2015.1110963.

[85] Z. Y. Liu, X. Z. Wang, C. W. Du, J. K. Li, X. G. Li, Effect of hydrogen-induced plasticity on the stress corrosion cracking of X70 pipeline steel in simulated soil environments, Materials Science and Engineering A 658 (2016) 348–354. doi:10.1016/j.msea.2016.02.019.

[86] CSA, CSA Z662-2011: Oil and Gas Pipeline Systems, Technical Report, Canadian Standards Association, Mississauga, Ontario, Canada, 2011.

[87] M. Nagumo, Fundamentals of Hydrogen Embrittlement, Springer, Tokyo, 2016. doi:10.1007/978-981-10-0161-1.

[88] D. A. Horner, B. J. Connolly, S. Zhou, L. Crocker, A. Turnbull, Novel images of the evolution of stress corrosion cracks from corrosion pits, Corrosion Science 53 (2011) 3466–3485. doi:10.1016/j.corsci.2011.05.050.